

DISSERTATION

ELECTRICAL IMPEDANCE TOMOGRAPHY RECONSTRUCTIONS
IN TWO AND THREE DIMENSIONS: FROM CALDERÓN TO
DIRECT METHODS

Submitted by

Jutta Bikowski

Department of Mathematics

In partial fulfillment of the requirements

for the degree of Doctor of Philosophy

Colorado State University

Fort Collins, Colorado

Spring 2009

UMI Number: 3374679

INFORMATION TO USERS

The quality of this reproduction is dependent upon the quality of the copy submitted. Broken or indistinct print, colored or poor quality illustrations and photographs, print bleed-through, substandard margins, and improper alignment can adversely affect reproduction.

In the unlikely event that the author did not send a complete manuscript and there are missing pages, these will be noted. Also, if unauthorized copyright material had to be removed, a note will indicate the deletion.

UMI[®]

UMI Microform 3374679
Copyright 2009 by ProQuest LLC
All rights reserved. This microform edition is protected against
unauthorized copying under Title 17, United States Code.

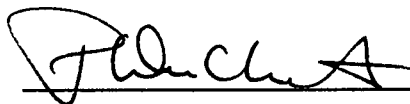
ProQuest LLC
789 East Eisenhower Parkway
P.O. Box 1346
Ann Arbor, MI 48106-1346

COLORADO STATE UNIVERSITY

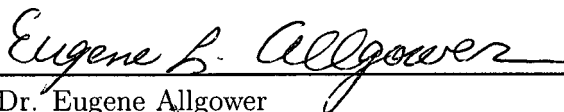
December 4, 2008

WE HEREBY RECOMMEND THAT THE DISSERTATION PREPARED UNDER OUR SUPERVISION BY JUTTA BIKOWSKI ENTITLED "ELECTRICAL IMPEDANCE TOMOGRAPHY RECONSTRUCTIONS IN TWO AND THREE DIMENSIONS; FROM CALDERÓN TO DIRECT METHODS" BE ACCEPTED AS FULFILLING IN PART REQUIREMENTS FOR THE DEGREE OF DOCTOR OF PHILOSOPHY.

Committee on Graduate Work



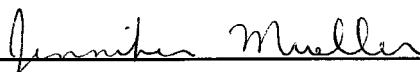
Dr. Paul DuChateau



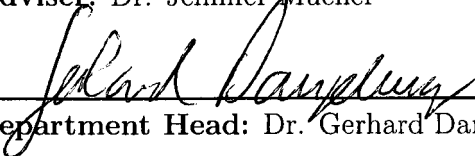
Dr. Eugene Allgower



Dr. Diego Krapf



Adviser: Dr. Jennifer Mueller



Department Head: Dr. Gerhard Dangelmayr

ABSTRACT OF DISSERTATION

ELECTRICAL IMPEDANCE TOMOGRAPHY RECONSTRUCTIONS IN TWO AND THREE DIMENSIONS: FROM CALDERÓN TO DIRECT METHODS

Electrical Impedance Tomography (EIT) uses voltage and current measurements from the boundary to reconstruct the electrical conductivity distribution inside an unknown object. In this dissertation two different EIT reconstruction algorithms are investigated. The first was introduced by A. P. Calderón [*Soc. Bras. de Mat.*, (1980), pp. 65-73]. His method was implemented and successfully applied to both numerical and experimental data in two dimensions, including a phantom that models a cross section of a human chest and data taken from a human chest.

The second algorithm is a non-iterative method that solves the full nonlinear problem and was introduced by A. Nachman [*Ann. of Math.*, 128 (1988), pp 531-576] for three or more dimensions. A version of this method was implemented and applied to spherically symmetric conductivity distributions. It is demonstrated that the t^{exp} -approximation to the scattering transform, which worked very well in two dimensions, does not represent an accurate estimate of the actual scattering transform near the origin. Therefore it has limited potential for reconstructions, especially since it is

also shown that the scattering transform near the origin has a strong influence on the reconstructions of the conductivity distribution. However, high quality reconstructions can be computed from knowledge of the scattering transform near the origin.

Jutta Bikowski
Department of Mathematics
Colorado State University
Fort Collins, Colorado 80523
Spring 2009

ACKNOWLEDGEMENTS

This research was possible thanks to the help and support of many people. First I want to thank my adviser Jennifer Mueller for all the time that she made available for me, for all her support, encouragement and guidance. Moreover I am grateful for all who were willing to listen to me and helped with comments and ideas. There are the faculty members from the department of mathematics of CSU: Gene Allgower, Paul DuChateau, Gerhard Dangelmayr and Jiangguo Liu. There are also the collaborators with my advisor and I: Samuli Siltanen, David Isaacson and Kim Knudsen who were always helpful.

A special thanks goes to all my friends who supported me in many different ways. This includes my office mates who were always willing to listen, my climbing and hiking friends who helped me to balance life, and the people from church who reminded me of the important parts of life.

Last but not least I thank my parents, Anneliese and Erich.

TABLE OF CONTENTS

1	Introduction	1
1.1	What is Electrical Impedance Tomography?	1
1.2	Applications	3
1.3	The Mathematical Formulation of the Problem	4
1.4	Uniqueness	5
1.5	Reconstructions	6
1.6	This Work in the Context of EIT Research	10
2	2D EIT Reconstructions using Calderón's Method	14
2.1	The Theory of the Reconstruction Method	14
2.1.1	The Set-up and Notation	14
2.1.2	Calderón's Reconstruction Method	15
2.2	Practical Aspects of Calderón's Method	19
2.3	Calderón's Method - Results	22
2.3.1	The Radially Symmetric Case	22
2.3.2	Tank Data	27
2.3.3	Chest Data	29
2.4	Conclusion	31
3	A 3D Direct Reconstruction Method	33
3.1	The Outline of the Reconstruction Method	33
3.1.1	Step 1: Changing the Problem into the Analogous Schrödinger Equation	34
3.1.2	Step 2: Finding the Nonphysical Scattering Transform $t(\xi, \zeta)$	35
3.1.3	Step 3: Recovering the Schrödinger Potential q from t	40
3.1.4	Step 4: Determining the Conductivity γ from q	41
3.2	Implementation Building Blocks	43
3.2.1	Expansions with Spherical Harmonics	44
3.2.2	The Fourier Transform and its Discretization	47
3.2.3	Eigenvalues and Eigenfunctions of the DtN Map	50
3.2.4	Eigenvalues of a Smooth Conductivity Distribution	56
3.2.5	Choosing ξ and ζ	58
3.3	Implementation of t^{exp} for Spherically Symmetric Conductivities	60

3.3.1	Symmetry	61
3.4	Implementation Details for Obtaining the Conductivity Distribution γ	62
3.5	Results	65
3.5.1	The Example	65
3.5.2	The Scattering Data	65
3.5.3	An Investigation of $t^{exp}(0)$	68
	Test of implemented routines	69
	Theoretical Considerations	72
3.5.4	The Schrödinger Potential	73
3.5.5	The Conductivity Distribution	74
3.5.6	The Influence of Different Parameters	75
	The Influence of the Truncation of the Scattering data	75
	The Influence of the Support of γ	77
	The Influence of the Magnitude of γ	77
3.6	Conclusion	79
3.7	Directions for Future Research	80
4	Summary	83
A	Calculation of the Error Bound in Calderón's method	85
	Bibliography	88

LIST OF FIGURES

2.1	Reconstructions of three radially symmetric conductivities . . .	25
2.2	Unmollified reconstructions with different truncation radii . . .	26
2.3	Reconstructions with different mollifier parameters	26
2.4	Phantom chest and its reconstruction	30
2.5	Reconstruction of 24 difference images of perfusion in a human chest, taken during breath-holding.	32
3.1	The integrand when taking the Fourier transform	48
3.2	Approximation of a smooth curve with step functions	57
3.3	Plots of different conductivity distributions	66
3.4	Scattering data	67
3.5	Reconstructions of the Schrödinger potential	74
3.6	Reconstructions of square root of conductivity distribution . . .	75
3.7	Reconstructions with different truncation of the scattering data	76
3.8	Reconstructions with different support of γ	78
3.9	Reconstructions with different support and magnitude of γ . .	79

Chapter 1

INTRODUCTION

1.1 What is Electrical Impedance Tomography?

Ultrasound, Magnetic Resonance Imaging (MRI), Computed Tomography (CT) and Emission Tomography (SPECT, PET) all have the purpose to ‘look inside’ an object without invasive methods. Each of these modalities makes use of different physical properties of the material under investigation. A very distinctive physical property is the electrical conductivity. This raises the question of whether we could use electrical conductivity to ‘look inside’ or, in other words, is it possible to determine the electrical conductivity of an unknown object through knowledge of current densities and voltages on the boundary. This is the so called conductivity problem. The range of applications is broad and includes, but is not restricted to, medical imaging, environmental science, and nondestructive testing of materials.

The idea of using electrical properties of materials is about 100 years old. In 1926 Ficke and Morse investigated the electrical properties of breast tumors [33] and the Schlumberger brothers used the idea for geophysical applications [70]. In medical applications the idea found some implementation in impedance phlebography, or impedance plethysmography (IPG) which measures small changes in electrical resistance which reflect blood volume changes. More recently, researchers work on imaging conductivity

distributions using current and voltage measurements from the boundary. This process is called Electrical Impedance Tomography, EIT, in medical applications or Electrical Resistance Tomography, ERT, in geophysical science¹. The foundation for EIT was laid by Calderón in 1980, [18]. He asked the question whether it is mathematically possible to find the conductivity distribution from voltage and current measurements on the boundary and if so how can this be done. Not only did he formulate the question in a mathematically rigorous framework, but also contributed to the answers. His article stimulated avid interest among researchers. The work in this dissertation is directly and indirectly inspired by Calderón.

We investigate in this thesis two different EIT reconstruction algorithms. The first was introduced by Calderón in [18]. We implemented Calderón's method and applied it successfully to numerical and experimental data, a phantom that models a cross section of a human chest and data taken from a human chest. A full description of this method and results are presented in chapter 2. The second algorithm was introduced in [62] for three or higher dimensions. It is a non iterative method that solves the full nonlinear problem. Following a similar approach as in 2D, see [67], we implemented this method and applied it to spherically symmetric conductivities distributions. Chapter 3 describes the details of this algorithm. The rest of this chapter gives more information about EIT in general and places the work in this dissertation in context with other research in EIT.

¹Since the author has mostly medical applications in mind it is called EIT in this thesis

1.2 Applications

One reason for the avid interest in the conductivity problem is certainly the broad range of applications which include medical imaging, geophysical applications, material testing and other industrial applications. A good overview of some applications is given in [20]. In the following we look at a few applications in medical imaging and show why they are promising.

Reliable breast cancer detection is still a challenge nowadays. The usual x-ray mammography has a specificity of about 60% and a sensitivity of 74%, [51]. It is desirable to increase these percentages. There are numerous studies about the different electrical properties of cancerous and healthy tissue in the breast. Even though particular values differ in these studies, the overall consensus is that the conductivity of malignant, benign and healthy tissue differs, [43]. So far there is one FDA approved imaging device that uses Electrical Impedance Imaging for breast cancer detection, the T-SCAN, [4]. There have been several studies on the use of the T-SCAN. For an overview see [43]. Moreover there are other research groups who developed EIT systems for the detection of breast cancer. To name just a few, see [22, 51, 23] and references within. All of these studies show promising results but need still some improvements to use them in a clinical setting.

Another challenging problem in medical imaging is to image and localize brain activity with noninvasive techniques. A conductivity increase can occur in the brain due to increase in the regional cerebral blood flow since blood has a higher conductivity, [34]. Similarly the conductivity can decrease due to cell swelling which decreases the inter cellular space that is

higher conductive. For some results on how EIT was used to monitor brain activity see [6, 73].

Other areas of applications that have been studied and showed encouraging results are monitoring lung and cardiac functionality and internal hemorrhage, see, for example [48, 32, 76, 1, 54] and [66], respectively.

Some of the advantages of EIT is that it is a noninvasive, low cost technique and it can be applied on a bedside, for example, in an ICU, without moving the patient. Moreover EIT could be combined with other imaging modalities to improve the quality of diagnostic tools.

1.3 The Mathematical Formulation of the Problem

Consider a bounded domain D in \mathbb{R}^n , $n \geq 2$ with Lipschitz boundary ∂D . Let γ be a bounded measurable function in D with positive lower bound $0 < \gamma_0 \leq \gamma(x)$ which represents the conductivity distribution. If $w(x) \in H^1(D)$ denotes the voltage (or potential) then the system is mathematically described as follows:

$$\nabla \cdot (\gamma(x)\nabla w) = 0, \quad w|_{\partial D} = f \quad (1.1)$$

where f is the trace of the voltage. The generalized Laplace equation, (1.1), can be derived from Maxwell's equation see, for example, [20]. The *forward problem* is to find the current density $j(x) = \gamma(x)\frac{\partial w(x)}{\partial \nu}|_{\partial D}$ on the boundary given that the conductivity distribution $\gamma(x)$ and the voltage on the boundary, $f(x)$, are known. This problem is well studied and in some cases even analytically solvable. Let the Dirichlet-to-Neuman (DtN) map, Λ_γ be defined by

$$\Lambda_\gamma f = \gamma(x) \frac{\partial w}{\partial \nu} \Big|_{\partial D}$$

where $f \in H^{1/2}(\partial D)$ agrees with w on the boundary. The DtN map is associated with the voltage to current density map. The *inverse conductivity problem* can now be stated as 'Given the knowledge of the DtN map is it possible to find the conductivity distribution $\gamma(x)$?' More precisely this involves two separate questions:

1. Given two DtN maps that are identical does this imply that the conductivity distributions are identical? (uniqueness question)
2. How can we find γ from measurements? (reconstruction question)

1.4 Uniqueness

The first answer to the uniqueness question came from Calderón. He found that the linearized problem is injective; that is, the linearization about $\gamma = 1$ uniquely determines γ . However, since the range of the linearized DtN map is not closed, we can not conclude injectivity of the original problem. After Calderón many researchers have worked on the uniqueness question. It would be too lengthy to list all results. For a good overview for results prior to 1999, see [74]. For more current results, see [5] and references there in. Here we mention only a few important results and the ones that are currently the sharpest. Kohn and Vogelius showed 1985 in [53] that Λ_γ uniquely determines γ for piecewise analytic γ 's and $\partial D \in C^\infty$. The first global uniqueness result goes back to Sylvester and Uhlmann in 1987 [72] who proved that Λ_γ uniquely determines $\gamma(x) \in C^\infty(\bar{D})$, $x \in \mathbb{R}^n$, $n \geq 3$ if $\partial D \in C^\infty$. Since then, the conditions on γ were more and more relaxed and currently the sharpest result for three and higher dimensions is for $\gamma \in W^{3/2,p}(D)$ with $p > 2n$ by Brown and Torres [17]. The 2D case remained unsolved until Nachman showed uniqueness for ∂D Lipschitz and

$\gamma \in W^{2,p}(D), p > 1$ in 1996 [63] and recently uniqueness in two dimensions was shown for $\gamma \in L^\infty$ by Astala and Päiväranta [5]. All the results mentioned above are for isotropic materials with conductivities bounded and bounded away from zero. Counterexamples with degenerate conductivities can be found in [37, 38]. These examples started a new line of research: invisibility, cloaking and wormholes see, for example, [39].

1.5 Reconstructions

The affirmative answer to the uniqueness questions for non degenerate conductivities in isotropic materials is encouraging. Then the next question is: How can we reconstruct the conductivity distribution from measurements on the boundary? This turns out to be a difficult problem because the DtN map is nonlinear. Moreover it is an ill-posed problem in the sense of Hadamard, [40]. The third condition of Hadamard is not satisfied in general, which means the solution does not depend continuously on the data and is therefore ill-posed. In other words, small changes in the boundary values might be caused by large changes in the conductivity.

There are several approaches for reconstruction algorithms:

1. Linearization methods

In this group falls the reconstruction suggested by Calderón in [18]. The basis for linearization methods is the assumption that the conductivity does not deviate much from a given (usually constant) conductivity distribution. Let $F(\gamma)$ denote the forward operator that maps the conductivity distribution γ to a voltage and assume $\gamma(x) = \gamma_0 + \eta(x)$ where γ_0 is a constant conductivity and $\eta(x)$ is a perturbation with small magnitude. Then we can write

$$F(\gamma) = F(\gamma_0) + \mathbf{J}(\eta) + O(\eta^2). \quad (1.2)$$

If η is small, then we can neglect the terms of order η^n for $n \geq 2$ to obtain a linearization of F . Rewriting equation (1.2), we get a relation between the changes in the potential and the changes in the conductivity

$$\delta w = \mathbf{J}\eta \tag{1.3}$$

where δw is the change in the voltage on the boundary. Most of the linearization algorithms calculate in some way the matrix \mathbf{J} , often called the sensitivity matrix, and then solve the system given in (1.3). This system is ill-posed due to the nature of the problem. Hence to find the solution is not a trivial task and requires some kind of regularization. Linearization methods are usually relatively easy to implement but the problem with them is the assumption that the conductivity is a small perturbation of a constant conductivity. Because of this, the actual conductivity values that display medium to high contrast are not well reconstructed with linearization algorithms. On the other hand, the conductivity values are not needed if we are interested in the change of conductivity over time. Therefore, linearization methods are good at detecting these changes.

Linearization methods were applied to EIT reconstructions right from the beginning, see [18] and [7] with references therein. They also can be found in more recent work, especially in 3 dimensional problems, [59, 23, 58] and in real time application. There are many linearization-based algorithms including back projection methods [8, 9, 65], moment methods [2], one-step Newton methods, such as the NOSER algorithm [21] and others [10, 12, 59].

2. Iterative methods

Iterative methods redefine the problem into an optimization problem. The cost function, g , which should be minimized is given by

$$g = \min_{\gamma} \|W_m - F(\gamma)\|^2 \quad (1.4)$$

where W_m is the measured voltage and F the forward operator. As in many optimization problems a regularization term is added which results in

$$g = \min_{\gamma} \|W_m - F(\gamma)\|^2 + G(\gamma).$$

where G could be many different functions but a typical one is $G(\gamma) = \alpha^2 \|\mathbf{L}(\gamma - \gamma_{ref})\|^2$ where \mathbf{L} is a discrete version of a differential operator and γ_{ref} is some reference conductivity, such as a conductivity distribution that is assumed to be similar as the expected conductivity. There are still some challenges. First of all that method requires the forward solution. For complicated domains, such as a human head, solving the forward problem can be a computationally intensive task and many papers are devoted to the question of how reconstruction algorithms can be improved by improving the forward solution, see [75]. Another problem is the usual difficulty with optimization problems that we might find a local minimum and the convergence rate might be slow. Some iterative methods can be found in [13, 14, 26, 27, 28, 50, 75, 36].

3. Bayesian Methods

Bayesian methods are statistical methods in which all variables are treated as random variables and in particular the conductivity distribution γ becomes a random variable Γ . The goal is to find the

posterior distribution $\pi(\Gamma|d)$ conditional on the data by using the likelihood function $\pi(d, \Gamma)$ and some prior(s) $\pi_{pr}(\Gamma)$ containing a-priori information about γ . The last step is to explore $\pi(\Gamma|d)$, often done with Markov Chain Monte Carlo (MCMC) methods. Such methods were used in [77, 49, 64, 56].

4. Direct methods

A direct method is a method that solves the full nonlinear problem without iteration. Layer stripping is one method that is considered a direct method [69, 71, 78]. The idea is that the conductivity is determined layer by layer going from the boundary to the center of the domain. Even though each layer depends on the reconstruction of the previous layer, it is not iterative since for each point in space there is only one calculation. Layer-stripping methods prove to be extremely unstable and are therefore not used in applications.

Another class of direct methods are the so called $\bar{\partial}$ -methods. These are based on ideas from inverse scattering and involve the computation of a type of nonlinear Fourier transform called the scattering transform. To determine the conductivity distribution from the scattering data an equation involving the $\bar{\partial}$ derivative² of an intermediate function needs to be solved, and this gives the method its name. A $\bar{\partial}$ -bar method was given Nachman in [63] for two dimensional objects. Successful implementations of this method for two dimensions are documented in [48, 60, 67]. A $\bar{\partial}$ -bar method for three dimensional

²The derivative with respect to the complex conjugate.

problems was published in [24]. The scattering transform for 3D domains was already used and described in detail by Nachman in [62]. For an implementation of the 3D problem see chapter 3.

1.6 This Work in the Context of EIT Research

The mathematical interest in EIT started with Calderón's seminal paper [18]. This article is probably the most cited article in the EIT literature and is known for formulating the conductivity problem in a rigorous mathematical setting. However, little attention has been paid to the reconstruction method that was proposed in that work. It could be argued that his algorithm is applicable to conductivities containing small perturbations, but that is true for all linearization methods which are widely used.

In this work we implemented Calderón's algorithm. To our knowledge this is the first implementation for experimental data of the method proposed by Calderón. In [19] Isaacson and Isaacson apply the method to radially symmetric conductivities with a jump discontinuity from Neumann-to-Dirichlet data and provide an insightful explicit formulation of the reconstructed conductivity. In [46] Isaacson and Cheney study the effects of finite measurement precision and limited number of electrodes on a 2-D version of Calderón's method with Neumann-to-Dirichlet data. In [52] a connection to the D-bar method is revealed, and Calderón's method is applied to the same type of conductivity as in [19] from Dirichlet-to-Neumann data and an explicit formulation of the reconstructed conductivity is also given. Here we show how to apply the method to two dimensional experimental data in a stable manner and demonstrate it to be both fast and useful for practical applications. After this work was published, a three dimension

variant of Calderón's method was implemented and successfully applied to experimental data by Boverman et al. in [15].

Linearization methods are usually very efficient but as the name already suggests they do not take the nonlinear nature of the problem into account. This limits the quality of the reconstructions which means that we need to turn to other methods. Most common are iterative methods which have been well explored. Bayesian and direct methods show promising results, but they have not been studied as thoroughly.

A first implementation of a 2D $\bar{\partial}$ -method was published in 2000 [67] which included examples of radially symmetric conductivity distributions. The same algorithm was successfully applied to experimental data acquired from a phantom chest [47] and from a human chest [48]. The second part of this thesis investigates an implementation of a direct method for 3D EIT reconstructions introduced by A. Nachman in [62]. The algorithm is applied to spherically symmetric conductivities.

Most implementations of EIT reconstructions, including the work in [69, 49, 48], are for two dimensional domains. For example, the authors of [11, 48] consider a cross section of the chest and consequently reduce a 3D object to two dimensions. As a next step some methods divide the problem into a stack of 2D problems. This has the benefit that the already tried and tested 2D algorithm can be used but it does not take the current flow between the slices into account. Even though the major current flow is between the electrodes it is not correct to assume that the current flow in the third dimension is negligible. Therefore, a full 3D algorithm would be beneficial for more accuracy. An experimental justification of the benefits of a full 3D reconstruction algorithm is given in [41].

Still, there are relatively few algorithms that consider the full 3D problem. One reason is the computational cost. All reconstruction algorithms divide the domain into small regions (voxels) over which the conductivity is assumed to be constant and then reconstruct the conductivity for all regions. Note that some reconstructions, for example linearizations have restrictions on the number of voxels depending on the number of electrodes used. By restriction we mean that more voxels would not improve the reconstruction, but rather decrease the quality of the result since it makes the problem more ill conditioned. In the following discussion we assume that we either do not have such restriction or we do not exhaust the number of voxels.

There is a trade-off between resolution and computational intensity. We want the voxels to be small for a good resolution of the resulting image. But smaller voxels imply more voxels which is computationally more expensive. Moreover, for 3D objects we have many more voxels than for 2D objects which increases the amount of calculations.

Let us demonstrate this on an example: Consider square domains and divide each side into 4 subintervals. For a square we have $4^2 = 16$ regions, but for a box we get $4^3 = 64$, which is four times as much as the square. More dramatically, dividing each side into 100 subintervals, the square has 100^2 regions, whereas the box has 100^3 . Now consider that for each of these regions we need to calculate the conductivity, and we can see how the calculations for 3D objects get very large very quickly.

A first step toward an implementation of a direct 3D algorithm makes up the second part of this thesis. The theoretical foundation of this algorithm goes back to Nachman [62] and has similarities to the two dimensional

algorithm [63]. Interesting is that the theory of the 3D algorithm was published 8 years before the 2D method but the implementation of the 3D method started about 8 years later than the 2D implementation.

The very elegant idea to use $\bar{\partial}$ methods for reconstructing conductivities, as is used in 2D, did not appear in [62]. The problem is the possibility of exceptional points³. A large step toward such a method was done by Cornean et. al. [24] where the authors showed the nonexistence of exceptional points if $|\zeta|$ is small, where ζ is a vector of complex variables⁴. This result enables the authors to formulate a $\bar{\partial}$ -equation for 3D.

As mentioned above, the thesis consists of two parts. Chapter 2 describes Calderón's method, its implementation for two dimensional domains, and presents the resulting reconstructions for numerical and experimental data. A description and first implementation of a 3D direct reconstruction method can be found in Chapter 3 which ends with a discussion of the results.

³See section 3.1.2 for explanation of exceptional points

⁴For more details on ζ see section 3.1.2

Chapter 2

2D EIT RECONSTRUCTIONS USING CALDERÓN'S METHOD

In his seminal work [18] Calderón considers the question of whether the conductivity distribution γ is uniquely determined by the knowledge of the DtN map, Λ_γ , and if so, how to calculate γ . Even though the idea of using electrical boundary measurements to find information about an unknown object was not completely new, Calderón was the first who put the problem in a rigorous mathematical framework. In addition, he showed that the linearized problem is uniquely determined by the DtN map and provided a reconstruction method for conductivities distributions that are small perturbations of a constant conductivity. We took Calderón's idea and implemented the reconstruction algorithm and applied it to numerical and experimental data. In this chapter we describe the theoretical background, some details from the implementation and present the reconstructions of this linearization method.

2.1 The Theory of the Reconstruction Method

2.1.1 The Set-up and Notation

Consider the set up and the differential operator, L_γ described in equation (1.1) of section 1.3. For the DtN map Calderón uses the quadratic form given by

$$Q_\gamma(f) = \int_D \gamma |\nabla w|^2 dx, \quad w \in H^1(\mathbb{R}^n), \quad w|_{\partial D} = f. \quad (2.1)$$

and with the condition $L_\gamma w = 0$ in D .

$$\begin{aligned} Q_\gamma(f) &= \int_D \gamma |\nabla w|^2 dx = \int_{\partial D} \gamma w \nabla w \cdot \nu d\sigma - \int_D (\nabla \cdot \gamma \nabla w) w dx \\ &= \int_{\partial D} \gamma \frac{\partial w}{\partial \nu} w d\sigma \end{aligned} \quad (2.2)$$

Let us introduce some notation that is used throughout Calderón's paper. Let $w = u + v$ where $\Delta u = L_1 u = 0$ and $u|_{\partial D} = \Phi$. Since $w|_{\partial D} = \Phi$, then $v|_{\partial D} = 0$ and hence $v \in H_0^1(D)$. Moreover, since $L_\gamma w = 0$, it is straightforward to see that

$$0 = L_{1+\delta} w = L_\delta u + L_1 v + L_\delta v. \quad (2.3)$$

Calderón chose to use two specific exponentially growing harmonic functions

$$u_1(x) = e^{\pi i(z \cdot x) + \pi(a \cdot x)} \quad \text{and} \quad u_2(x) = e^{\pi i(z \cdot x) - \pi(a \cdot x)} \quad (2.4)$$

where $a, z \in \mathbb{R}^n$ with $z \cdot a = 0$ and $|z| = |a|$. He makes the important assumption that γ is a constant plus a perturbation $\delta(x)$, and for convenience sets the constant to 1 so that $\gamma(x) = 1 + \delta(x)$.

2.1.2 Calderón's Reconstruction Method

Calderón starts with the fomulation of a bilinear form,

$$B(f_1, f_2) = \frac{1}{2} [Q_\gamma(w_1 + w_2) - Q_\gamma(w_1) - Q_\gamma(w_2)]. \quad (2.5)$$

Again, let $w_i = u_i + v_i$ with $i = 1, 2$ and $\Delta u_i = L_1 u_i = 0$, $u_i|_{\partial D} = \Phi_i$ and let $\gamma = 1 + \delta$. Since $u_i|_{\partial D} = w_i|_{\partial D}$ it follows that $v_i|_{\partial D} = 0$. By using the definition of Q , (2.1),

$$\begin{aligned}
B(f_1, f_2) &= \frac{1}{2} \int_D \gamma (|\nabla w_1|^2 + 2\nabla w_1 \cdot \nabla w_2 + |\nabla w_2|^2) \\
&\quad - \gamma |\nabla w_1|^2 - \gamma |\nabla w_2|^2 dx \\
&= \frac{1}{2} \int_D 2\gamma (\nabla w_1 \cdot \nabla w_2) dx \\
&= \int_D \gamma (\nabla(u_1 + v_1) \cdot \nabla(u_2 + v_2)) dx \\
&= \int_D \gamma (\nabla u_1 \cdot \nabla u_2 + \nabla u_1 \cdot \nabla v_2 + \nabla v_1 \cdot \nabla u_2 + \nabla v_1 \cdot \nabla v_2) dx \\
&= \int_D (1 + \delta) (\nabla u_1 \cdot \nabla u_2 + \nabla v_1 \cdot \nabla v_2) \\
&\quad + \delta (\nabla u_1 \cdot \nabla v_2 + \nabla v_1 \cdot \nabla u_2) dx. \tag{2.6}
\end{aligned}$$

As the notation already suggests we will use the exponentially growing functions u_1 and u_2 from (2.4) which gives us $\nabla u_1 \cdot \nabla u_2 = -2\pi^2 |z|^2 e^{2\pi(z \cdot x)}$. Dividing equation (2.6) by $-2\pi^2 |z|^2$ yields

$$\hat{\gamma}(z) = \hat{F}(z) + R(z) \tag{2.7}$$

where

$$\begin{aligned}
\hat{\gamma}(z) &= -\frac{1}{2\pi^2 |z|^2} \int_D (1 + \delta) \nabla u_1 \cdot \nabla u_2 dx \\
&= -\frac{1}{2\pi^2 |z|^2} \int_D \gamma e^{2\pi i(z \cdot x)} dx \\
\hat{F}(z) &= -\frac{1}{2\pi^2 |z|^2} B(e^{i\pi(z \cdot x) + \pi(a \cdot x)}, e^{i\pi(z \cdot x) - \pi(a \cdot x)}) \\
R(z) &= \frac{1}{2\pi^2 |z|^2} \int_D \delta (\nabla u_1 \cdot \nabla v_2 + \nabla v_1 \cdot \nabla u_2) \\
&\quad + (1 + \delta) \nabla v_1 \cdot \nabla v_2 dx. \tag{2.8}
\end{aligned}$$

If γ is extended to be zero outside D , then $\hat{\gamma}(z)$ can be interpreted as the Fourier transform of γ . $\hat{F}(z)$ can in principle be determined from the

measured data because it is given by the bilinear form (2.5) which is related to our measured DN data through (2.2).

Now we need to take care of the term $R(z)$. Calderón shows that $R(z)$ is bounded if the perturbation δ is small. In particular he shows that

$$|R(z)| \leq C \|\delta\|_\infty^2 e^{2\pi|z|r} \quad (2.9)$$

where C is a constant and r is the radius of the smallest sphere containing the domain¹. Appendix A shows the derivation of the bound in detail. Note that this error can grow exponentially as z gets large. Therefore we consider the special case when

$$|z| \leq \frac{2-\alpha}{2\pi r} \log \frac{1}{\|\delta\|_\infty} =: \sigma \quad (2.10)$$

where α is a constant between 1 and 2. With this specific z we have

$$\begin{aligned} |R(z)| &\leq C \|\delta\|_\infty^2 e^{2\pi r \frac{2-\alpha}{2\pi r} \log \frac{1}{\|\delta\|_\infty}} \\ &= C \|\delta\|_\infty^2 e^{\log(\frac{1}{\|\delta\|_\infty})^{2-\alpha}} \\ &= C \|\delta\|_\infty^2 \|\delta\|_\infty^{\alpha-2} \\ &= C \|\delta\|_\infty^\alpha. \end{aligned} \quad (2.11)$$

This error bound enables us to say that $\hat{F}(z)$ is a good approximation for $\hat{\gamma}$ provided δ is small. Note that if z is too large the error will be large. In the reconstructions it can be observed that the algorithm becomes unstable for larger values of z .

Since $\gamma \in L^\infty$ it is desirable to apply a mollifier η to avoid a Gibb's phenomenon in the inversion of the Fourier transform. The mollifier, η , is a

¹Provided that $A\|\delta\|_\infty < 1 - \epsilon$ where A is the norm of the inverse of the operator L_1 .

compactly supported smooth function on \mathbb{R}^n with $\int_{\mathbb{R}^n} \eta(y) dy = 1$. It decays exponentially which implies that the Fourier transform of the mollifier, $\hat{\eta}$, is in C^∞ . Moreover the support of $\hat{\eta}$ is in $\{z : |z| \leq 1\}$ and $\hat{\eta}(0) = 1$. The usual properties of the Fourier transform give $\hat{\eta}\left(\frac{z}{\sigma}\right) = \sigma^n \eta(\sigma x) =: \eta_\sigma(x)$. There are several functions that satisfy these properties but in this work we used $\eta_\sigma(x) = \sigma^n e^{-\pi|\sigma x|^2}$ where n is the dimension. Equation (2.7) becomes

$$\hat{\gamma}(z)\hat{\eta}\left(\frac{z}{\sigma}\right) = \hat{F}(z)\hat{\eta}\left(\frac{z}{\sigma}\right) + R(z)\hat{\eta}\left(\frac{z}{\sigma}\right).$$

Taking the inverse Fourier transform results in

$$(\gamma * \eta_\sigma)(x) = (F * \eta_\sigma)(x) + \rho(x) \quad (2.12)$$

where $*$ denotes convolution. A bound for ρ can be found in the following way.

$$|\rho(x)| = \left| \int_{\mathbb{R}^n} R(z) \hat{\eta}\left(\frac{z}{\sigma}\right) e^{-2\pi i z \cdot x} dz \right| \leq \int_{\mathbb{R}^n} C \|\delta\|_\infty^\alpha \left| \hat{\eta}\left(\frac{z}{\sigma}\right) \right| dz$$

by (2.11). Since $\hat{\eta}$ is supported on $B_\sigma \equiv \{z : \left|\frac{z}{\sigma}\right| \leq 1\}$,

$$\int_{\mathbb{R}^n} C \|\delta\|_\infty^\alpha \left| \hat{\eta}\left(\frac{z}{\sigma}\right) \right| dz = C \|\delta\|_\infty^\alpha \int_{B_\sigma} \left| \int_{\mathbb{R}^n} \sigma^n \eta(x\sigma) e^{2\pi i x \cdot z} dx \right| dz$$

The change of variables $y = \sigma x$, $dy = \sigma^n dx$ then gives an upper bound of

$$C \|\delta\|_\infty^\alpha \int_{B_\sigma} \left| \int_{\mathbb{R}^n} \sigma^n \eta(x\sigma) e^{2\pi i x \cdot z} dx \right| dz \leq C \|\delta\|_\infty^\alpha \int_{B_\sigma} \left| \int_{\mathbb{R}^n} \eta(y) dy \right| dz$$

which, by properties of η becomes

$$C \|\delta\|_\infty^\alpha \int_{B_\sigma} dz = C_1 \|\delta\|_\infty^\alpha \sigma^n$$

where $\int_{B_\sigma} dz = \text{Vol}(B_\sigma) = \text{constant} \cdot \sigma^n$. By 2.10 this is bounded above by

$$C_1 \|\delta\|_\infty^\alpha \left(\log \frac{1}{\|\delta\|_\infty} \right)^n \quad (2.13)$$

where C_1 depends only on the domain D , α and ϵ .² If we now let $\|\delta\|_\infty = t$ be very small then repeated applications of L'Hospital's Rule yield

$$\lim_{t \rightarrow 0} t^\alpha \left(\log \frac{1}{t} \right)^n = \lim_{t \rightarrow 0} \frac{\left(\log \frac{1}{t} \right)^n}{t^{-\alpha}} = \lim_{t \rightarrow 0} \frac{n \left(\log \frac{1}{t} \right)^{n-1}}{\left(\frac{-\alpha}{t^\alpha} \right)} = \dots = \lim_{t \rightarrow 0} \frac{t^\alpha n!}{(-\alpha)^n} = 0 \quad (2.14)$$

which shows that the error goes to zero if $\delta \rightarrow 0$.

With this error bound we can neglect ρ in equation (2.12) for small δ 's and say

$$\gamma(x) \approx (\gamma * \eta_\sigma)(x) \approx (F * \eta_\sigma)(x) \quad (2.15)$$

which gives the idea for Calderón's reconstruction method.

2.2 Practical Aspects of Calderón's Method

To reconstruct $\gamma(x)$ using the Calderón approximation $(F * \eta_\sigma)(x)$, one must first approximate \hat{F} in (2.7) from the measured current-to-voltage data, multiply by a mollifying function η , and numerically invert the transform in the region of interest. We will derive an expression for \hat{F} in terms of a discrete matrix approximation \mathbf{L}_γ to the DtN map, Λ_γ . The discrete approximation will be defined below in section 2.3.2.

By (2.7) $\hat{F}(z)$ is given by

$$\hat{F} = -\frac{1}{2\pi^2|z|^2} B(\phi_1, \phi_2). \quad (2.16)$$

²The epsilon come from the condition $A\|\delta\|_\infty < 1 - \epsilon$ where A is the norm of the inverse of the operator L_1 .

and B is defined as in (2.5). Then

$$\begin{aligned}
B(\phi_1, \phi_2) &= \frac{1}{2} (Q_\gamma(\phi_1 + \phi_2) - Q_\gamma(\phi_1) - Q_\gamma(\phi_2)) \\
&= \frac{1}{2} \int_D \gamma |\nabla(w_1 + w_2)|^2 - \gamma |\nabla w_1|^2 - \gamma |\nabla w_2|^2 dx \\
&= \frac{1}{2} \int_D 2\gamma (\nabla w_1 \cdot \nabla w_2) dx \\
&= \int_{\partial D} w_1 \gamma \frac{\partial w_2}{\partial \nu} d\sigma = \int_{\partial D} w_1 \Lambda_\gamma w_2 d\sigma \tag{2.17}
\end{aligned}$$

since $\nabla \cdot \gamma \nabla w_1 = \nabla \cdot \gamma \nabla w_2 = 0$. Because the functions w_1 and w_2 are unknown, Calderón uses the functions u_1 and u_2 defined in (2.4). Note that $w_1|_{\partial D} = \phi_1 = u_1|_{\partial D}$ and $w_2|_{\partial D} = \phi_2 = u_2|_{\partial D}$. Equation (2.17) involves a boundary integral and hence we can use u_1 and u_2 . The next question is how to calculate $B(\phi_1, \phi_2)$ using the given measurements. For this we first express the values of u in terms of the basis functions $e^{in\theta}$ since here we consider reconstructions on a circular 2D domain.

Now suppose the domain is a disk with radius R and let $x|_{\partial D} = Re^{i\theta}$, $z = |z|e^{i\phi}$ and $a = |z|e^{i(\phi \pm \pi/2)}$ because $a \cdot z = 0$ and $|z| = |a|$. Then

$$\begin{aligned}
\pi(a \cdot x + i(z \cdot x))|_{\partial D} &= \pi|a|R \cos(\theta - (\phi \pm \pi/2)) + i\pi|z|R \cos(\theta - \phi) \\
&= |z|\pi R (\cos(\theta - \phi \mp \pi/2) + i \cos(\theta - \phi)) \\
&= |z|\pi R (\pm \sin(\theta - \phi) + i \cos(\theta - \phi)) \\
&= |z|\pi R i (\mp i \sin(\theta - \phi) + \cos(\theta - \phi)) \\
&= |z|\pi R i e^{\mp i(\theta - \phi)}
\end{aligned}$$

Now we can expand $u_1|_{\partial D}$:

$$\begin{aligned}
u_1|_{\partial D} &= e^{\pi(a \cdot x + i(z \cdot x))}|_{\partial D} = e^{|z|i\pi R e^{\mp i(\theta - \phi)}} \\
&= \sum_{j=0}^{\infty} \frac{(|z|i\pi R e^{\mp i(\theta - \phi)})^j}{j!} = \sum_{j=0}^{\infty} a_j(z) e^{\mp ij\theta}
\end{aligned}$$

where $a_j(z) = \frac{(|z|\pi R i e^{\pm i\phi})^j}{j!}$. Similarly $u_2|_{\partial D} = \sum_{j=0}^{\infty} b_j(z) e^{\pm i j \theta}$ where $b_j(z) = \frac{(|z|\pi R i e^{\mp i\phi})^j}{j!}$. Now using both expansions in equation (2.17) we get

$$\begin{aligned} Q_\gamma(\phi_1, \phi_2) &= Q_\gamma(u_1|_{\partial D}, u_2|_{\partial D}) = \int_{\partial D} u_1 \Lambda_\gamma u_2 d\sigma \\ &= \int_0^{2\pi} \sum_{j=0}^{\infty} a_j e^{\mp i j \theta} \Lambda_\gamma \sum_{k=0}^{\infty} b_k e^{\pm i k \theta} R d\theta \\ &= R \sum_{j=0}^{\infty} \sum_{k=0}^{\infty} a_j b_k \int_0^{2\pi} e^{\mp i j \theta} \Lambda_\gamma e^{\pm i k \theta} d\theta \end{aligned}$$

This gives an equation for \hat{F} :

$$\begin{aligned} \hat{F}(z) &= -\frac{1}{2\pi^2|z|^2} B(\phi_1, \phi_2) = -\frac{1}{2\pi^2|z|^2} Q(u_1|_{\partial D}, u_2|_{\partial D}) \\ &= \frac{-R}{2\pi^2|z|^2} \sum_{j=0}^{\infty} \sum_{k=0}^{\infty} a_j(z) b_k(z) \int_0^{2\pi} e^{\mp i j \theta} \Lambda_\gamma e^{\pm i k \theta} d\theta \quad (2.18) \end{aligned}$$

Note that in [46] a series formulation is given for the perturbation from a constant conductivity of 1 containing differences of Neumann-to-Dirichlet maps $R_0 - R_\gamma$ applied to $e^{in\theta}$ where R_0 is the map corresponding to a constant conductivity of 1. The calculation of the last integral in (2.18) depends on the experiment. In this thesis we consider three different settings:

1. The unit disk with radially symmetric inclusions centered at the origin. This is a purely numerical setting with no actual measured data. Similar tests were studied in [52].
2. Data collected on a circular tank with agar heart and lungs in a saline bath. The experiment is described in detail in section 2.3.2 and was also used with the D-bar method in [47].
3. Data collected on 32 electrodes placed around the circumference of a human chest. The experiment is described in detail in section 2.3.3 and was also used with the D-bar method in [48].

Once $\hat{F}(z)$ is determined it remains to apply the mollifier and to take the inverse Fourier transform. As a mollifying function we used $\eta_\sigma(x) = g_t(x) = te^{-\pi|x|^2/t}$ where $\sigma = 1/\sqrt{t}$. The Fourier transform is then $\hat{\eta}(z/\sigma) = \hat{g}_t(z) = e^{-\pi t|z|^2}$. The last step in the reconstructions is taking the inverse Fourier transform which was done with a straightforward Simpson's rule.

2.3 Calderón's Method - Results

In this section we present the results of applying Calderón's method to the three types of data described above. Noise-free simulated data from radially symmetric conductivities were also considered in [52] where a connection with the D-bar method [63, 67] was revealed. The reconstructions in [52] with Calderón's method are performed from an explicit series formulation for the reconstructed γ , which differs from this work in that here the Fourier transform is inverted numerically for all three data settings, as originally proposed by Calderón.

2.3.1 The Radially Symmetric Case

Three radially symmetric conductivities with jump discontinuities and no noise are considered. They have the following general form

$$\gamma(x) = \begin{cases} \gamma_1 & \text{for } |x| \leq r_1, \\ \gamma_2 & \text{for } r_1 < |x| \leq r_2, \\ 1 & \text{for } r_2 < |x| \leq R. \end{cases} \quad (2.19)$$

where $0 < r_1 < r_2 < R$ and $\gamma_i > 0, i = 1, 2$. These examples are on the unit disk with $\gamma = 1$ on ∂D , but could be as well more general. Example 1 has one circular inclusion centered at the origin with radius $r_2 = 0.35$ and conductivity $\gamma_i = 1.3, i = 1, 2$. Example 2 has two jump discontinuities, at $r_1 = 0.3$ and at $r_2 = 0.6$, with conductivities $\gamma_1 = 0.8$ and $\gamma_2 = 1.3$.

In Example 3 we consider a conductivity with a very high contrast jump discontinuity ($\gamma_i = 99, i = 1, 2$ at $r_2 = .35$) that is outside the scope of Calderón's assumptions to demonstrate that the method is still effective in locating the radius of the jump.

For the radially symmetric case the trigonometric functions $e^{in\theta}$ are eigenfunctions of the Dirichlet-to-Neumann map [71]. The corresponding eigenvalues λ_n for the case of a single constant inclusion on a unit disk as in Examples 1 and 3 are given by [35]

$$\lambda_n = n \left(1 + \frac{2\alpha r^{2n}}{1 - \alpha r^{2n}} \right), \quad n = 1, 2, 3, \dots \quad (2.20)$$

where $\alpha = \frac{\gamma-1}{\gamma+1}$. A formula for the eigenvalues in the case of multiple concentric inclusions, as in Example 2, is given in [67]. Note that if $R \neq 1$ then the eigenvalues must be divided by R since the Dirichlet-to-Neumann map on the unit disk, $\Lambda_{\gamma,1}$ is related to the Dirichlet-to-Neumann map on a disk of radius r , $\Lambda_{\gamma,r}$ by $r\Lambda_{\gamma,r} = \Lambda_{\gamma,1}$. Using these facts in (2.18) gives

$$\hat{F}(z) = \frac{-R}{2\pi^2|z|^2} \sum_{j=0}^{\infty} \sum_{k=0}^{\infty} a_j b_k \frac{\lambda_{\pm k}}{R} \int_0^{2\pi} e^{i(\mp j \pm k)\theta} d\theta = \frac{-1}{2\pi^2|z|^2} 2\pi \sum_{k=0}^{\infty} a_k b_k \lambda_k \quad (2.21)$$

which can be explicitly calculated.

In the radially symmetric case we do not truncate the series as in [46], but rather we use some simplifications to determine the inverse Fourier transform. Let $\hat{F}_m(z)$ denote the mollified version of $\hat{F}(z)$. That is, $\hat{F}_m(z) = \hat{F}(z)\hat{\eta}_t(z)$. Let ϕ denote the angle between z and x . Then

$$\begin{aligned} \int_{-\infty}^{\infty} \int_{-\infty}^{\infty} \hat{F}_m(z) e^{i2\pi z \cdot x} dz_1 dz_2 &= \int_0^{\infty} \hat{F}_m(r) \left(\int_0^{2\pi} e^{i2\pi r \cdot x} d\theta \right) r dr \\ &= \int_0^{\infty} \hat{F}_m(r) \left(\int_0^{2\pi} e^{i2\pi r|x|\cos\phi} d\phi \right) r dr \end{aligned}$$

According to [55] Section 3.2.1 $e^{i\alpha \cos(\beta)} = \sum_{n=-\infty}^{\infty} i^n e^{in\beta} J_n(\alpha)$ where $J_n(\alpha)$ are Bessel functions of the first kind. Thus,

$$\begin{aligned} \int_{-\infty}^{\infty} \int_{-\infty}^{\infty} \hat{F}_m(z) e^{i2\pi z \cdot x} dz &= \int_0^{\infty} \hat{F}_m(r) \int_0^{2\pi} \sum_{n=-\infty}^{\infty} i^n e^{in\phi} J_n(2\pi r|x|) d\phi r dr \\ &= \int_0^{\infty} \hat{F}_m(r) J_0(2\pi r|x|) 2\pi r dr \end{aligned}$$

since $\int_0^{2\pi} e^{in\phi} d\phi = 0$ if $n \neq 0$. Thus, neglecting the remainder term in (2.12) and truncating the integration at T_z gives the reconstruction formula

$$\gamma(x) \approx \int_0^{T_z} \hat{F}_m(r) J_0(2\pi r|x|) 2\pi r dr. \quad (2.22)$$

Equations (2.21) and (2.22) give a complete description of the reconstruction method. There are no further regularization methods necessary. One can regard the truncation of z and the application of the mollifier as regularizations.

The integration in (2.22) was computed with a composite Simpson's rule. Cross-sectional plots of the radially symmetric conductivities and the reconstructions are found in Figure 2.1. The dotted line indicates the actual conductivity values and the solid curve is the reconstruction. The plots in figure 2.1 were computed with a truncation radius of $T_z = 5$ and a mollifier parameter of $t = .03$.

The reconstructed curve tends to zero near $r = 1$ because in the reconstruction algorithm we extended the domain and set $\gamma = 0$ outside the domain, as explained above in equation (2.8).

In each case, the location of the jump is well-reconstructed. This is consistent with our expectations since the explicit series representation of the reconstructed γ given in [52] contains a term pinpointing the exact location of the jump. The magnitude is severely underestimated in the

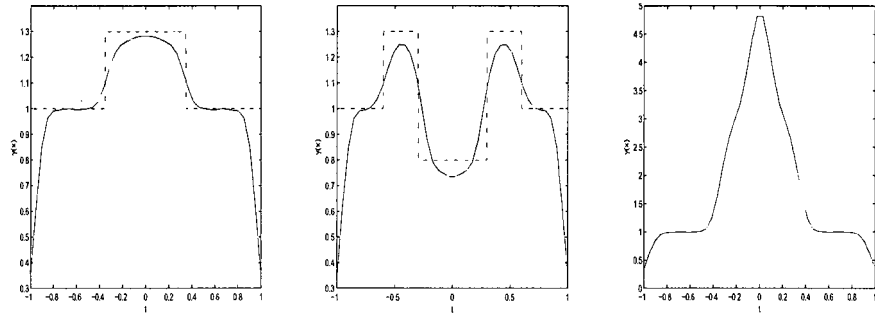


Figure 2.1: Reconstructions of three radially symmetric conductivities given by equation (2.19). The dotted line in the first two plots are the actual conductivities. The third plot does not include the actual conductivity since its magnitude is $\gamma_1 = 100$, much larger than the reconstructed magnitude.

high contrast example 3, but this is to be expected since the underlying assumption of the method is that the conductivity is a small perturbation from a constant.

In numerical calculations we cannot evaluate the inverse Fourier transform over the entire space; we have to truncate z . Moreover, Calderón shows that the error bound of the neglected remainder term grows exponentially with z . The influence of the truncation radius can be seen in figure 2.2 where Example 1 is reconstructed with no mollifier and by truncating the parameter z at truncation radius $T_z = 4, 5, 6, 7$. If the truncation radius gets too large the reconstruction becomes unstable, which was to be expected. In this numerical example, we are separating the effects of the truncation radius and the mollification on the reconstruction. In the theoretical analysis in [46] these effects are considered together in the effect of the mollifier function. They conclude that the blurring error is made smallest by choosing a mollifying function as narrowly peaked as possible.

For our choice of mollifier, that corresponds to decreasing t . Note, however, that due to the Gibbs' phenomenon, we cannot allow t to go to zero.

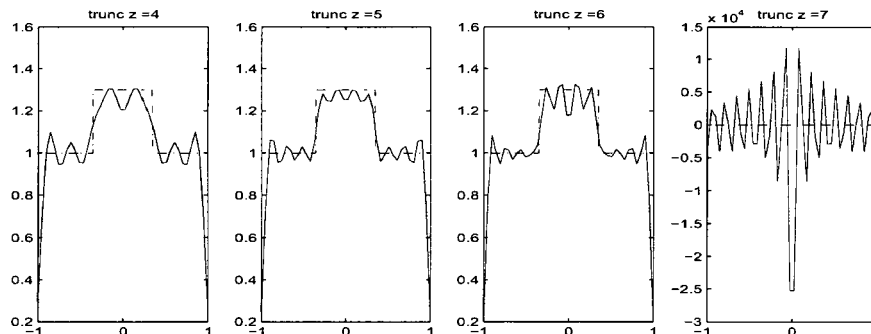


Figure 2.2: Unmollified reconstructions of Example 1 with different truncation radii, $T_z = 4, 5, 6, 7$.

In figure 2.3 the mollified function \hat{F}_m is inverted with truncation radius $T_z = 7$. Increasing the parameter t in the mollifier increases the amount of smoothing of \hat{F} and hence reduces the oscillations in the reconstructed approximation $\gamma * \eta$. As seen in figure 2.3, the reconstruction is quite sensitive to the value of t , but by including the mollifier, computations with somewhat larger truncation radii become quite feasible.

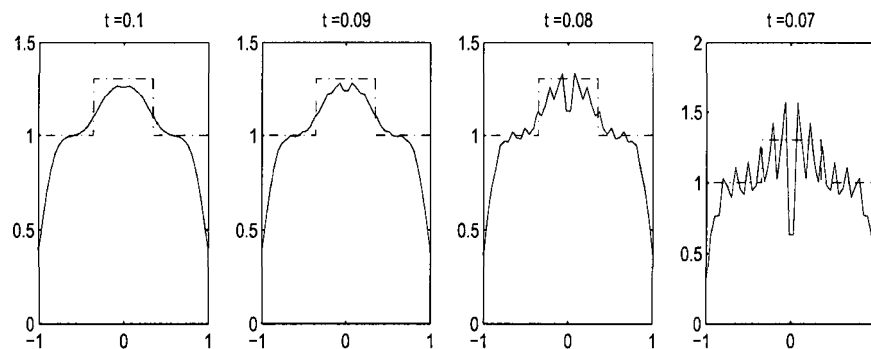


Figure 2.3: Reconstructions of Example 1 with truncation radius $T_z = 7$ for different mollifier parameters, $t = 0.1; 0.09; 0.08; 0.07$.

2.3.2 Tank Data

For setting 2 the same experimental data as in [47] was used. Currents were applied on 32 electrodes of size 1.6 cm high and 2.5 cm wide on a circular phantom chest with a 15 cm radius containing two agar lungs (240mS/m) and an agar heart (750 mS/m) in a saline bath (424mS/m) and the corresponding voltages were measured. The measurements were collected using the ACT3 system at Rensselaer Polytechnic Institute [29]. In the experiment trigonometric current patterns with a current amplitude M of 0.2 mA peak-to-peak were applied at a frequency of 28.8 kHz. Let L denote the number of electrodes, e_l the l th electrode, and $\theta_l = 2\pi l/L$ the angle of the center of the l th electrode. Let T_l^k be the current applied on the l th electrode in the k th current pattern, and T^k the vector of these values for current pattern k . Then the trigonometric current patterns applied in this experiment are given by

$$T_l^k = \begin{cases} M \cos(k\theta_l), & k = 1, \dots, \frac{L}{2} - 1 \\ M \cos(\pi l), & k = \frac{L}{2} \\ M \sin((k - L/2)\theta_l), & k = \frac{L}{2} + 1, \dots, L - 1 \end{cases} \quad (2.23)$$

One challenge with experimental data is the calculation of (2.18) since the integral $\int_{\partial D} e^{\pm ij\theta} \Lambda_\gamma e^{\pm ik\theta} dx$ is unknown but implicitly given by the measured data. A similar calculation was performed in [47], and we refer to that work, where possible. Let \mathbf{L} denote the discrete Dirichlet-to-Neumann matrix with entries given by $\mathbf{L}_{\mathbf{m},\mathbf{n}} = \left(c_l^{\mathbf{m}}, \left(\frac{R_\gamma}{A} \right)^{-1} c_l^{\mathbf{n}} \right)_L$ where $c_l^{\mathbf{n}}$ is an orthonormal basis for the vector space spanned by the applied current patterns and R_γ is the current-to-voltage operator corresponding to a conductivity γ in a disk of radius r . Here the currents span the space \mathbb{R}^{L-1} and $c^{\mathbf{m}} = \frac{T^{\mathbf{m}}}{\|T^{\mathbf{m}}\|^2}$. Modeling the current density j on the boundary with the ‘‘ave-gap model’’,

[68], we let

$$j^k(x, y) = \begin{cases} \frac{T_l^k}{A_l}, & (x, y) \in e_l \\ 0, & \text{otherwise} \end{cases}$$

where A_l is the size of the l th electrode (which we will henceforth denote by A since the electrodes are uniform in size). Let $\Delta\theta = 2\pi/L$ be the angle between the center of the electrodes. Now from [47], discretizing the integral and applying Euler's formula gives

$$\begin{aligned} & \int_0^{2\pi} e^{\pm im\theta} \Lambda_\gamma e^{\pm in\theta} d\theta \\ & \approx \frac{A}{\Delta\theta} \langle e^{im\theta}, \Lambda_\gamma(e^{in\theta})(\theta) \rangle \approx \frac{\Delta\theta}{A} (e^{im\cdot}, \left(\frac{R_\gamma}{A}\right)^{-1} (e^{in\cdot}))_L \\ & = (\cos m\cdot, \left(\frac{R_\gamma}{A}\right)^{-1} (\cos n\cdot))_L + i(\cos m\cdot, \left(\frac{R_\gamma}{A}\right)^{-1} (\sin n\cdot))_L \\ & \quad - i(\sin m\cdot, \left(\frac{R_\gamma}{A}\right)^{-1} (\cos n\cdot))_L + (\sin m\cdot, \left(\frac{R_\gamma}{A}\right)^{-1} (\sin n\cdot))_L \\ & \approx \frac{\|T^m\|_2 \|T^n\|_2}{M^2} \mathbf{L}_{m,n} + i \frac{\|T^m\|_2 \|T^n\|_2}{M^2} \mathbf{L}_{m,L/2+n} \\ & \quad - i \frac{\|T^m\|_2 \|T^n\|_2}{M^2} \mathbf{L}_{L/2+m,n} + \frac{\|T^m\|_2 \|T^n\|_2}{M^2} \mathbf{L}_{L/2+m,L/2+n} \end{aligned} \quad (2.24)$$

with $1 \leq n, m \leq L/2$ and the two inner products defined as $\langle f, g \rangle = \int_0^{2\pi} \overline{f(\theta)} g(\theta) d\theta$ and $(u(\cdot), w(\cdot))_L = \sum_{l=1}^L \overline{u(\theta_l)} w(\theta_l)$. Applying this to equation (2.18) we have

$$\begin{aligned} \hat{F}(z) &= \frac{-R}{2\pi^2 |z|^2} \sum_{j=0}^{\infty} \sum_{k=0}^{\infty} a_j b_k \int_0^{2\pi} e^{\mp ij\theta} \Lambda_\gamma e^{\pm ik\theta} d\theta \\ &\approx \frac{-R}{2\pi^2 |z|^2} \frac{L\Delta\theta}{2A} \\ &\quad \left(\sum_{j=1}^{L/2-1} \sum_{k=1}^{L/2-1} a_j b_k \left(\mathbf{L}_{j,k} + \mathbf{L}_{\frac{L}{2}+j, \frac{L}{2}+k} + i \left(\mathbf{L}_{j, \frac{L}{2}+k} - \mathbf{L}_{\frac{L}{2}+j, k} \right) \right) \right. \\ &\quad + \sqrt{2} \sum_{k=1}^{\frac{L}{2}-1} a_{\frac{L}{2}} b_k \left(\mathbf{L}_{\frac{L}{2}, k} + i \mathbf{L}_{\frac{L}{2}, \frac{L}{2}+k} \right) + \sqrt{2} \sum_{j=1}^{\frac{L}{2}-1} a_j b_{\frac{L}{2}} \left(\mathbf{L}_{j, \frac{L}{2}} - i \mathbf{L}_{\frac{L}{2}+j, \frac{L}{2}} \right) \\ &\quad \left. + 2(-1)^{\frac{L}{2}} a_{\frac{L}{2}} b_{\frac{L}{2}} \mathbf{L}_{\frac{L}{2}, \frac{L}{2}} \right). \end{aligned} \quad (2.25)$$

Once we have $\hat{F}(z)$ we multiply it with the mollifying function $\eta_\sigma(z) = g_t(z) = te^{-\pi|z|^2/t}$ where we set $t = 0.05$ and take the inverse Fourier transform, using Simpson's rule, to obtain the reconstruction of γ . The truncation radius was chosen to be $T_z = 4.3/(R\pi) \approx .00912$ where R is the radius of the tank in mm. The dependence of T_z on the tank radius is due to the factors $a_j(z) = \frac{(|z|\pi Rie^{\pm i\phi})^j}{j!}$ and $b_k(z) = \frac{(|z|\pi Rie^{\mp i\phi})^k}{k!}$ in equation (2.18). The reconstructed image can be seen in figure 2.4. The reconstruction was computed on a coarse grid (31x31) and interpolated to a finer grid (200x200) for a smooth looking plot. In the reconstruction the location of the heart and the lungs can be seen, but with some significant distortion of the heart. However, the difference in the sizes of the lung is recognizable in the reconstruction and a clear separation exists between the left and right lung. The relative error in the heart region is 5.37%, where the maximum conductivity value in the heart region is used. In the lung region, it is 91.66%, where the minimal conductivity value in the lung region is used. Increasing the mollification has the effect of reducing the error in the lung region and increasing it in the heart region.

2.3.3 Chest Data

The last set of reconstructions is based on human chest data acquired by placing 32 electrodes 29 mm high by 24 mm wide around a human chest and recording 100 different measurements during breath-holding at 18 frames/sec. The data used here is archival data measured by the ACT3 system at Rensselaer Polytechnic Institute, and is the same data used in [48]. Trigonometric current patterns with amplitude $M = 0.85$ mA were applied and the chest was modeled as a disk of radius $r = 14.3$ cm, corresponding to a 90 cm circumference.

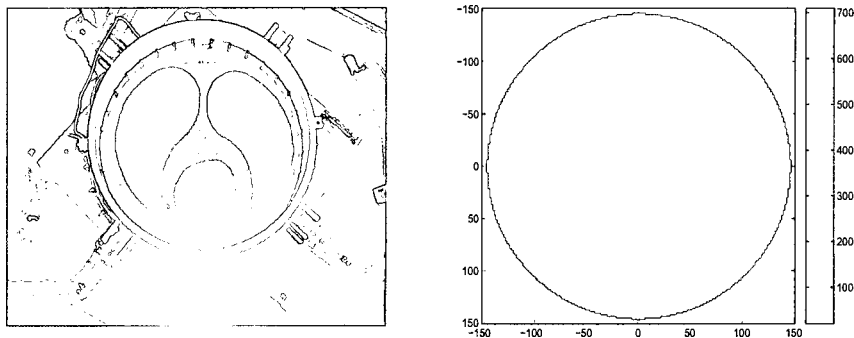


Figure 2.4: On the left is a photo of the phantom chest. On the right is an absolute image showing the reconstruction using Calderón's method in units of mS/m.

Difference images were computed by first differencing the discrete Dirichlet-to-Neumann matrices for each image with a reference data set. One frame in the data sequence (halfway between systole and diastole) was chosen as a reference image, and the discrete Dirichlet-to-Neumann map for this reference image was subtracted from the discrete Dirichlet-to-Neumann map for each frame. Since the reconstruction formula (2.18) is linear, this is mathematically equivalent to subtracting the reconstruction of the reference frame from each reconstruction in the sequence. A sequence of 24 reconstructions are shown in figure 2.5. In each image of that figure, dorsal is at the top, ventral is at the bottom, and the subject's left is on the viewer's right. These reconstructions were calculated with a truncation radius of $T_z = 4/(143\pi) \approx .0089$, no mollifier was used, and the inverse Fourier transform was calculated with a two dimensional Simpson rule. Considering several reconstructed difference images it can be seen how the heart changes conductivity between systole and diastole. The depicted 24 reconstructions in figure 2.5 represent approximately one cardiac cycle, about 1.33s. It starts mid systole when the highly conductive blood is pumped from the

heart into the adjacent lungs, making them more conductive. Therefore, the lung region appears red in the first 3 or 4 reconstructions. Then in the beginning of diastole the heart starts to fill with blood again and becomes more conductive which can be seen starting at 5th reconstruction. At the same time the lungs are less conductive than the heart and are therefore blue. Since diastole accounts for 13/18 of the cardiac cycle it last much longer than systole. At about the 22nd reconstruction, the beginning of systole, it can be observed that the heart contracts suddenly, the blood gets pumped into the body and the conductivity of the heart also decreases abruptly. A movie of the whole reconstructed sequence in color can be viewed at

http://www.math.colostate.edu/~mueller/cardiacsequence_calderon.

2.4 Conclusion

Calderón's method can be applied to numerical and experimental data and gives promising results in the sense that conductivity changes are well reconstructed in terms of spatial resolution and even conductivity magnitude for medium contrast perturbations. Moreover the method does not require much computational effort and can therefore be easily implemented, and reconstructions can be obtained in very short computational time.

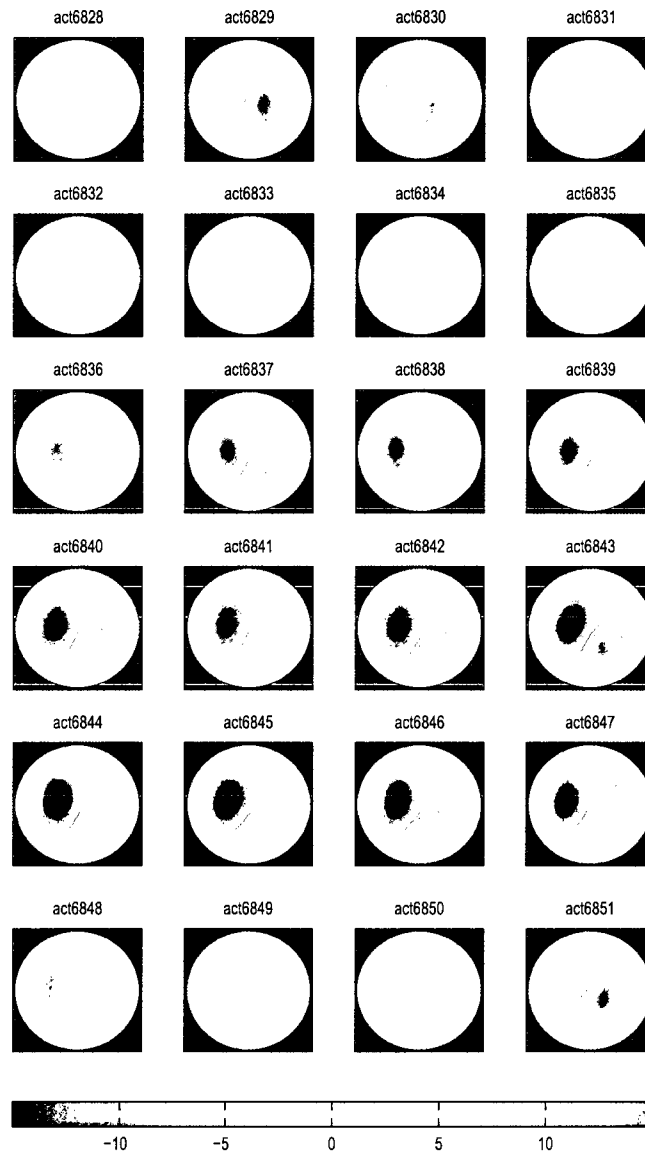


Figure 2.5: Reconstruction of 24 difference images of perfusion in a human chest, taken during breath-holding.

Chapter 3

A 3D DIRECT RECONSTRUCTION METHOD

In 1988 Nachman published an outline of an algorithm to reconstruct the conductivity distribution γ from measurements on the boundary for dimension three and higher. This method is a direct method which means that it solves the full nonlinear problem without iterations. In 1996 Nachman introduced a similar method for two dimensions, [63] which was successfully implemented for numerical and experimental data, [48], [47], [67]. Yet the three dimensional case remained open for implementation. The following chapter describes the implementation of Nachman's method. First I outline the algorithm, then I introduce some tools that are needed, followed by a description of an approximation for the scattering data which was implemented for spherically symmetric conductivities. At the end I show and discuss the results.

3.1 The Outline of the Reconstruction Method

The proposed reconstruction algorithm from Nachman can be divided into four steps, which are

1. Changing the problem into the analogous Schrödinger equation.

2. Finding the nonphysical scattering transform $t(\xi, \zeta)$.
3. Recovering the Schrödinger potential q from t
4. Determining the conductivity γ from q

Each of the steps is now described in more details.

3.1.1 Step 1: Changing the Problem into the Analogous Schrödinger Equation

Suppose $\gamma(x) \in C^{1,1}(\bar{D})$ where $C^{1,1}$ denotes the space of functions whose first derivatives satisfy a locally uniform Lipschitz condition. Moreover, let $0 < \gamma(x)$ for all $x \in D$ and D be a bounded domain in $\mathbf{R}^n, n \geq 3$ with $C^{1,1}$ boundary. Then the given problem $\nabla \cdot \gamma \nabla w = 0$ with $w|_{\partial D} = f$ can be converted into a Schrödinger equation with the substitution $u = \gamma^{\frac{1}{2}} w$ and $q = \gamma^{-\frac{1}{2}} \Delta \gamma^{\frac{1}{2}}$ as follows

$$\begin{aligned}
0 &= \nabla \cdot \gamma \nabla w \\
&= \gamma \Delta w + \nabla(\sqrt{\gamma} \sqrt{\gamma}) \cdot \nabla w \\
&= \gamma \Delta w + (\sqrt{\gamma} \nabla \sqrt{\gamma} + \sqrt{\gamma} \nabla \sqrt{\gamma}) \cdot \nabla w \\
&= -\sqrt{\gamma} \Delta w - 2 \nabla \sqrt{\gamma} \cdot \nabla w \\
&= -\sqrt{\gamma} \Delta w - \nabla \sqrt{\gamma} \cdot \nabla w - w \Delta \sqrt{\gamma} - \nabla \sqrt{\gamma} \cdot \nabla w + w \Delta \sqrt{\gamma} \\
&= -\nabla \cdot \sqrt{\gamma} \nabla w - \nabla \cdot (w \nabla \sqrt{\gamma}) + w \Delta \sqrt{\gamma} \\
&= -\nabla \cdot (\nabla \sqrt{\gamma} w) + w \Delta \sqrt{\gamma} \\
&= -\Delta(\sqrt{\gamma} w) + \Delta \sqrt{\gamma} \frac{\sqrt{\gamma}}{\sqrt{\gamma}} w \\
&= -\Delta u + qu
\end{aligned} \tag{3.1}$$

and q is called the Schrödinger potential and is an $L^\infty(D)$ function. The boundary condition $w|_{\partial D} = f$ translates into $u|_{\partial D} = \sqrt{\gamma} w|_{\partial D} = \sqrt{\gamma} f \equiv g$

and the new Dirichlet to Neumann map is $\Lambda_q g = \frac{\partial u}{\partial \nu} \Big|_{\partial D}$. The two DtN maps are related as follows, see [62] equation (1.34a),

$$\Lambda_q = \gamma^{-1/2} \Lambda_\gamma \gamma^{-1/2} + \frac{1}{2} \gamma^{-1} \frac{\partial \gamma}{\partial \nu}$$

This can be verified with the same substitution used in (3.1)

$$\begin{aligned} \Lambda_q g &= \frac{\partial u}{\partial \nu} \Big|_{\partial D} \\ &= \frac{\partial(\sqrt{\gamma} w)}{\partial \nu} \Big|_{\partial D} \\ &= \sqrt{\gamma} \frac{\partial w}{\partial \nu} \Big|_{\partial D} + w \frac{\partial \sqrt{\gamma}}{\partial \nu} \Big|_{\partial D} \\ &= \gamma^{-1/2} \gamma \frac{\partial \gamma^{-1/2} u}{\partial \nu} \Big|_{\partial D} + \gamma^{-1/2} u \frac{\partial \sqrt{\gamma}}{\partial \nu} \Big|_{\partial D} \\ &\quad \text{Note: } \frac{\partial \gamma}{\partial \nu} = \frac{\partial \gamma^{1/2} \gamma^{1/2}}{\partial \nu} = 2\gamma^{1/2} \frac{\partial \gamma^{1/2}}{\partial \nu} \\ &= \gamma^{-1/2} \gamma \frac{\partial \gamma^{-1/2} u}{\partial \nu} \Big|_{\partial D} + \frac{1}{2} \gamma^{-1/2} \gamma^{-1/2} u \frac{\partial \gamma}{\partial \nu} \Big|_{\partial D} \\ &= (\gamma^{-1/2} \Lambda_\gamma \gamma^{-1/2} + \frac{1}{2} \gamma^{-1} \frac{\partial \gamma}{\partial \nu}) g \end{aligned}$$

Note that if $\gamma = 1$ in a small neighborhood of the boundary, then $\Lambda_q = \Lambda_\gamma$. In the context of this work we use only conductivities that satisfy this condition. This implies that we use Λ_q and Λ_γ interchangeably. Moreover, we will use Λ_1 for the DtN map with constant conductivity of one and equivalently Λ_0 for the DtN map of the Schrödinger potential equal to zero, which corresponds to a constant conductivity.

3.1.2 Step 2: Finding the Nonphysical Scattering Transform $t(\xi, \zeta)$

The definition of the nonphysical scattering transform uses certain exponentially growing functions, also called complex geometric optics. Calderón already used exponentially growing functions to reconstruct con-

ductivities close to a constant in [18]. Later, Sylvester and Uhlmann extended the use of exponentially growing solutions to show uniqueness for $\gamma \in C^\infty(\bar{D})$, [72]. More specifically, Uhlmann and Sylvester as well as Nachman worked with solutions $\psi(x, \zeta)$ of

$$-\Delta\psi(x, \zeta) + q\psi(x, \zeta) = 0 \quad \text{in all } \mathbb{R}^n \quad (3.2)$$

where we introduce a new variable $\zeta \in \mathbb{C}^n$ and non real. Moreover, we require $\psi \sim e^{i\zeta \cdot x}$ for $|\zeta|$ large and $\zeta^2 = 0$. The solutions $\psi(x, \zeta)$ can be determined by solving an equivalent integral equation

$$\psi(x, \zeta) = e^{i\zeta \cdot x} - \int_{\mathbb{R}^n} G_\zeta(y - x)q(y)\psi(y, \zeta) dy. \quad (3.3)$$

with the Faddeev's Green's function

$$G_\zeta(x) \equiv \frac{1}{(2\pi)^n} e^{i\zeta \cdot x} \int_{\mathbb{R}^n} \frac{e^{i\zeta \cdot \xi}}{\xi^2 + 2\zeta \cdot \xi} d\xi.$$

which was introduced in [31] by Faddeev. To show that $G_\zeta(x)$ is a fundamental solution we first show that $g(x, \zeta) = \frac{1}{(2\pi)^n} \int_{\mathbb{R}^n} \frac{e^{i\zeta \cdot \xi}}{\xi^2 + 2\zeta \cdot \xi} d\xi$ is a fundamental solution for the operator $-\Delta - 2i\zeta \cdot \nabla$. That is, we need to show that $\langle -(\Delta + 2i\zeta \cdot \nabla)g, u \rangle = \langle \delta, u \rangle = u(0)$.

$$\begin{aligned} -(\Delta_x + 2i\zeta \cdot \nabla_x)g &= \frac{1}{(2\pi)^n} \left(\int_{\mathbb{R}^n} \frac{\xi^2 e^{i\zeta \cdot \xi}}{\xi^2 + 2\zeta \cdot \xi} d\xi + \int_{\mathbb{R}^n} \frac{2\zeta \cdot \xi e^{i\zeta \cdot \xi}}{\xi^2 + 2\zeta \cdot \xi} d\xi \right) \\ &= \frac{1}{(2\pi)^n} \int_{\mathbb{R}^n} \frac{(\xi^2 + 2\zeta \cdot \xi) e^{i\zeta \cdot \xi}}{\xi^2 + 2\zeta \cdot \xi} d\xi \\ &= \frac{1}{(2\pi)^n} \int_{\mathbb{R}^n} e^{i\zeta \cdot \xi} d\xi \\ \langle -(\Delta + 2i\zeta \cdot \nabla)g, u \rangle &= \int_{\mathbb{R}^n} \left(\frac{1}{(2\pi)^n} \int_{\mathbb{R}^n} e^{i\zeta \cdot \xi} d\xi \right) u(x) dx \\ &= \int_{\mathbb{R}^n} \left(\frac{1}{(2\pi)^n} \int_{\mathbb{R}^n} e^{i\zeta \cdot \xi} u(x) dx \right) d\xi \\ &= \int_{\mathbb{R}^n} \left(\frac{1}{(2\pi)^n} \int_{\mathbb{R}^n} e^{i\zeta \cdot \xi} u(x) dx \right) e^{-i0 \cdot \xi} d\xi \\ &= \mathcal{F}(\mathcal{F}^{-1}(u))_0 \\ &= u(0) = \langle \delta, u \rangle \end{aligned}$$

Considering $-\Delta G(x, \zeta) = -\Delta(e^{ix \cdot \zeta} g(x, \zeta)) = e^{ix \cdot \zeta}(-\Delta - 2i\zeta \nabla)g(x, \zeta)$ and using the last results we have

$$\begin{aligned}
\langle -\Delta G(x, \zeta), u(x) \rangle &= \langle e^{ix \cdot \zeta}(-\Delta - 2i\zeta \nabla)g(x, \zeta), u \rangle \\
&= \langle (-\Delta - 2i\zeta \nabla)g(x, \zeta), e^{-ix \cdot \zeta} u \rangle \\
&= \langle \delta, e^{-ix \cdot \zeta} u \rangle \\
&= e^{-i0 \cdot \zeta} u(0) = u(0) \\
&= \langle \delta, u \rangle
\end{aligned}$$

which shows that $G(x, \zeta)$ is a fundamental solution to the Laplace equation.

In order to work with the solutions of equation (3.3) we need to make sure that such solutions exist. If there is no function $\psi(x, \zeta)$ that satisfies equation (3.3) for a particular ζ , then we call this an exceptional point. Since we will define the scattering data in terms of these exponentially growing solutions, we need to make sure that we do not have exceptional points. Nachman showed in [62] there are no exceptional points for ζ sufficiently large.

The scattering transform is then defined in terms of these exponentially growing solutions,

$$t(\xi, \zeta) \equiv \int e^{-ix \cdot (\xi + \zeta)} q(x) \psi(x, \zeta) dx. \quad (3.4)$$

The Schrödinger potential $q(x)$ is unknown when we reconstruct the conductivity. Therefore we need an expression for the scattering data $t(\xi, \zeta)$ that does not depend explicitly on $q(x)$. Using $q\psi = \Delta\psi$ from equation

(3.2) and Green's identity leads to

$$\begin{aligned}
t(\xi, \zeta) &= \int_D e^{-ix \cdot (\xi + \zeta)} \Delta \psi(x, \zeta) dx \\
&= \int_{\partial D} e^{-ix \cdot (\xi + \zeta)} \frac{\partial \psi(x, \zeta)}{\partial \nu} d\sigma(x) \\
&\quad + \int_D i(\xi + \zeta) e^{-ix \cdot (\xi + \zeta)} \cdot \nabla \psi(x, \zeta) dx \\
&= \int_{\partial D} \left(e^{-ix \cdot (\xi + \zeta)} \frac{\partial \psi(x, \zeta)}{\partial \nu} + i(\xi + \zeta) \cdot \nu e^{-ix \cdot (\xi + \zeta)} \psi(x, \zeta) \right) d\sigma(x) \\
&\quad - \int_D (\xi + \zeta)^2 e^{-ix \cdot (\xi + \zeta)} \psi(x, \zeta) dx \\
&\quad \text{with } (\xi + \zeta)^2 = 0 \\
&= \int_{\partial D} e^{-ix \cdot (\xi + \zeta)} \left[\frac{\partial}{\partial \nu} + i(\xi + \zeta) \cdot \nu \right] \psi(x, \zeta) d\sigma(x) \tag{3.5} \\
&= \int_{\partial D} e^{-ix \cdot (\xi + \zeta)} [\Lambda_q \psi(x, \zeta) + i(\xi + \zeta) \cdot \nu \psi(x, \zeta)] d\sigma(x) \tag{3.6}
\end{aligned}$$

Note this is an expression for $t(\xi, \zeta)$ in terms of a boundary integral which implies that only values of ψ on the boundary of D are needed to calculate the scattering data. The only restriction is that ξ and ζ must satisfy $(\xi^2 + \zeta^2) = 0$. A slightly different representation can be obtained by using Alessandrini's identity, $\langle u_0(x), \Lambda_q - \Lambda_0 u(x) \rangle = \int_D q(x) u(x) u_0(x) dx$ with $u_0(x)$ a harmonic function. Setting $u(x) = \psi(x, \zeta)$ and $u_0(x) = e^{-ix \cdot (\xi + \zeta)}$ we can use Alessandrini's identity and we write

$$t(\xi, \zeta) = \int_{\partial D} e^{-ix \cdot (\xi + \zeta)} (\Lambda_q - \Lambda_0) \psi(x, \zeta) d\sigma(x) \tag{3.7}$$

assuming that $(\xi + \zeta)^2 = 0$ such that $e^{-ix \cdot (\xi + \zeta)}$ is harmonic. Both equations (3.6) and (3.7) are expressions for the scattering data $t(\xi, \zeta)$ in terms of boundary integrals not explicitly dependent on q . Not as obviously, we still have the unknown q in the expressions since it occurs in the definition of ψ . Nachman gives a remedy for that by showing that there are unique ψ

for $\zeta \in \mathbb{C}^n$ with $|\zeta|$ large and $\zeta^2 = 0$ if D is a bounded domain with a $C^{1,1}$ boundary¹, q real valued in $L^\infty(D)$ and zero not a Dirichlet eigenvalue of $-\Delta + q$, and these ψ 's can be determined on the boundary from Λ_q via

$$\psi(\cdot, \zeta) = e^{-ix \cdot \zeta} - \left(S_\zeta \Lambda_q - B_\zeta - \frac{1}{2} I \right) \psi(\cdot, \zeta) \quad (3.8)$$

where I is the identity operator,

$$S_\zeta f(x) = \int_{\partial D} G_\zeta(x, y) f(y) d\sigma(y)$$

is the single layer potential and

$$B_\zeta = p.v. \int_{\partial D} \frac{\partial G_\zeta(x, y)}{\partial \nu(y)} f(y) d\sigma(y)$$

is the generalized double layer potential. The two equations (3.6) and (3.8) relate the DtN map to the scattering data $t(\xi, \zeta)$.

For practical purposes we still have one difficulty. The calculation of ψ includes the single and double layer potential for which the Faddeev's Green's function is needed. An idea to avoid the difficult calculation of the Green's function is to use the asymptotic behavior $\psi \approx e^{ix \cdot \zeta}$ for $|\zeta|$ large. We established already that we need $|\zeta|$ large to make sure that we do not have exceptional points. Moreover, the 2D implementation of the $\bar{\delta}$ method uses a similar approximation (see [67, 48, 47]) and it was shown in [60] that in numerical experiments this approximation is close to the actual scattering data and reasonable reconstructions can be obtained from this approximation. When we use $\psi \approx e^{ix \cdot \zeta}$ we get an approximation of the

¹ $C^{1,1}$ denotes the space of functions whose first derivative satisfy a locally uniform Lipschitz condition.

scattering data which we denote by t^{exp}

$$\begin{aligned} t^{exp}(\xi, \zeta) &\equiv \int_{\partial D} e^{-ix \cdot (\xi + \zeta)} \left[\frac{\partial}{\partial \nu} + i(\xi + \zeta) \cdot \nu \right] e^{ix \cdot \zeta} d\sigma(x) \\ &= \int_{\partial D} e^{-ix \cdot (\xi + \zeta)} \Lambda_q e^{ix \cdot \zeta} + e^{-ix \cdot \xi} i(\xi + \zeta) \cdot \nu d\sigma(x) \end{aligned} \quad (3.9)$$

$$\text{or} = \int_{\partial D} e^{-ix \cdot (\xi + \zeta)} (\Lambda_q - \Lambda_0) e^{ix \cdot \zeta} d\sigma(x) \quad (3.10)$$

Using the approximation $t^{exp}(\zeta, \xi)$ reduces the calculation since the function $\psi(x, \zeta)$ is not needed anymore. Note that this approximation is taken for simplicity and in future work it would be good to use the function $\psi(x, \zeta)$, which should lead to more accurate results.

3.1.3 Step 3: Recovering the Schrödinger Potential q from t

In this step the scattering data $t(\xi, \zeta)$ is used to find the Schrödinger potential $q(x)$. The heart of this step is given by the bound

$$|t(\xi, \zeta) - \hat{q}(\xi)| \leq \frac{c(\delta, a)}{|\zeta|} \|q\|_\delta^2 \quad (3.11)$$

where $\hat{\cdot}$ indicates the Fourier transform and the weighted norm is given by $\|q\|_\delta^2 \equiv \int (1 + x^2)^\delta |q(x)|^2 dx$. The bound was explicitly given in [62] but the major work was already done in [72]. In the limit as $|\zeta|$ gets large we have

$$\lim_{|\zeta| \rightarrow \infty} t(\xi, \zeta) = \hat{q}(\xi).$$

Once we have $\hat{q}(\xi)$ we can take the inverse Fourier transform of it to get $q(x)$. More precisely,

$$\begin{aligned} q(x) &= \frac{1}{2\pi} \int_{\mathbb{R}^n} \hat{q}(\xi) e^{ix \cdot \xi} d\xi \\ &= \int_{\mathbb{R}^n} \hat{q}(2\pi\xi) e^{i2\pi x \cdot \xi} d\xi. \end{aligned}$$

Nachman outlines another approach using $\bar{\partial}_\zeta t$, the partial derivative of t with respect to ζ conjugate. The heart of this approach uses a version of

the Bochner-Martinelli formula, a special case of a theorem of Hatziafratis [42]. Even for this method the bound in (3.11) is used. Moreover, this method is computationally much more involved. This is the reason why we did not use this approach.

For conductivities close to a constant, Cornean et.al. suggest in [24] a method to reconstruct the conductivity γ using the scattering data $t(\xi, \zeta)$ for $|\zeta|$ small. The novelty of this approach is that they show that there are no exceptional points if ζ is small enough. Moreover, they do not calculate the Schrödinger potential directly. The idea from Cornean et. al. is the analogue of the 2D $\bar{\partial}$ -method which was implemented in [67, 60].

3.1.4 Step 4: Determining the Conductivity γ from q

In the last step we need to solve $q = \gamma^{-\frac{1}{2}} \Delta \gamma^{\frac{1}{2}}$. The idea is that we can write

$$\begin{aligned} \Delta \sqrt{\gamma} &= q \sqrt{\gamma} & (3.12) \\ \sqrt{\gamma}|_{\partial D} &= g(x) \end{aligned}$$

and then use the standard Green's function for Laplace's equation to solve for $\sqrt{\gamma}$. Note that in the context of this work $g(x) = 1$ because we assumed that $\gamma \equiv 1$ close to the boundary. In 3D the fundamental solution of the Laplace equation is given by

$$\Phi(x) = \frac{1}{4\pi|x|}$$

see, for example, [30]. The solution to the Dirichlet boundary value problem (3.12) is

$$\begin{aligned} \sqrt{\gamma(x)} &= - \int_{\partial D} g(y) \frac{\partial \Phi(x-y) - v(x-y)}{\partial \nu} d\sigma(y) \\ &\quad - \int_D (\Phi(x-y) - v(x-y)) q(y) \sqrt{\gamma(y)} dy \end{aligned}$$

where $v(x)$ is a harmonic function. In this thesis we consider spherical domains and therefore $v(x)$ can be determined by the method of reflection which gives $v(x) = \frac{a}{|x|}\Phi(x^* - y)$ where a is the radius of the sphere and $x^* = \frac{a^2x}{|x|^2}$. Setting $G(x) = \Phi(x) - v(x)$ gives us the desired Green's function and leads to the integral equation

$$\begin{aligned}\sqrt{\gamma(x)} &= -\int_{\partial D} g(y) \frac{\partial G(x-y)}{\partial \nu} d\sigma(y) - \int_D G(x-y) q(y) \sqrt{\gamma(y)} dy \\ &= \frac{a^2 - |x|^2}{4\pi a} \int_{|y|=a} \frac{1}{|x-y|^3} d\sigma(y) \\ &\quad - \frac{1}{4\pi} \int_D \frac{1}{|x-y|} - \frac{a}{|x||x^*-y|} q(y) \sqrt{\gamma(y)} dy\end{aligned}$$

The first integral can be simplified by using spherical coordinates,

$$\begin{aligned}x &= \langle r \cos \theta \cos \phi, r \sin \theta \cos \phi, r \cos \theta \rangle \\ y &= \langle a \cos \theta' \cos \phi', a \sin \theta' \cos \phi', r \cos \theta' \rangle.\end{aligned}$$

Note that the integral only depends on the distance of x to the origin but not on the concrete location which means that the integral is independent of θ and ϕ . Setting $\theta = 0$ and $\phi = 0$ we get

$$\begin{aligned}|x-y|^3 &= (r^2 + a^2 - 2ra(\sin \theta \sin \theta' \cos(\phi - \phi') + \cos \theta \cos \theta'))^{3/2} \\ &= (r^2 + a^2 - 2ra \cos \theta')^{3/2}\end{aligned}$$

and the integral reduces to

$$\begin{aligned}
& \frac{a^2 - |x|^2}{4a\pi} \int_{|y|=a} \frac{g(y)}{|x-y|^3} d\sigma(y) \\
&= \frac{a^2 - r^2}{a4\pi} \int_0^\pi \int_0^{2\pi} \frac{1}{(r^2 + a^2 - 2ra \cos \theta')^{3/2}} \sin \theta' d\phi' d\theta' \\
&= \frac{a^2 - r^2}{2a} \int_0^\pi \frac{1}{(r^2 + a^2 - 2ra \cos \theta')^{3/2}} \sin \theta' d\theta' \\
& \quad u = r^2 + a^2 - 2ra \cos \theta' \text{ and } du = 2ra \sin \theta' d\theta' \\
& \quad u(0) = r^2 + a^2 - 2ar = (r - a)^2 \\
& \quad u(\pi) = r^2 + a^2 + 2ra = (r + a)^2 \\
&= \frac{a^2 - r^2}{2a2ra} \int_{u(0)}^{u(\pi)} \frac{1}{u^{3/2}} du \\
&= \frac{a^2 - r^2}{4ra^2} (-2)u^{-1/2} \Big|_{u(0)}^{u(\pi)} \\
&= -\frac{a^2 - r^2}{2ra^2} \left(\frac{1}{a+r} - \frac{1}{a-r} \right) \\
&= -\frac{a^2 - r^2}{2ra^2} \left(\frac{(a-r) - (a+r)}{a^2 - r^2} \right) \\
&= \frac{1}{a^2}
\end{aligned}$$

This leaves us with the integral equation

$$\sqrt{\gamma(x)} = \frac{1}{a} - \frac{1}{4\pi} \int_D \frac{1}{|x-y|} - \frac{a}{|x||x^* - y|} q(y) \sqrt{\gamma(y)} dy \quad (3.13)$$

The details of the implementation of this integral equation are described in section 3.4.

3.2 Implementation Building Blocks

In the implementation of the 3D reconstruction method we use different mathematical ideas and concepts which I call 'building blocks'. First we review some known methods such as spherical harmonics expansion and Fourier transform. Then we describe the tools that we developed specifically

for this problem. In the next section we bring it all together and describe the implementation of the approximation of the scattering data.

Before we go further we need a word about the examples that we have in mind. This work is about spherically symmetric conductivity distributions and some of the building blocks are specifically for these conductivity distributions. For more general γ 's we would need to adjust some of the tools. So for convenience we assume for the rest of this thesis that we have spherically symmetric conductivity distributions on a unit sphere and as mentioned earlier we assume that $\gamma \equiv 1$ close to the boundary. The unit sphere was chosen for convenience and everything can be generalized to spheres with arbitrary radius. Moreover, for different geometries we would need slightly different methods. This is an interesting task, but it is not considered in this context.

3.2.1 Expansions with Spherical Harmonics

For the calculation of the scattering transform we will expand functions in terms of spherical harmonics. I will use the normalized version

$$Y_l^m(\theta, \phi) = \sqrt{\frac{2l+1}{4\pi} \frac{(l-m)!}{(l+m)!}} P_l^m(\cos \theta) e^{im\phi} = N_l^m P_l^m(\cos \theta) e^{im\phi}$$

where P_n^m are associated Legendre functions and N_l^m is a normalization factor². These Y_l^m 's are orthonormal over spherical surfaces (see any text book with spherical harmonics for example [3]). Given the function $f_C(x) =$

²Note: Some sources have a factor of $(-1)^m$ in the normalization. It is possible to put it either in the normalization factor or in the associated Legendre functions. This factor is called the Condon-Shortley phase. Often it is included because it is more natural in some applications. I assume that the factor is in the associated Legendre functions just as Matlab does.

$e^{ix \cdot \zeta}$ for a fixed $\zeta \in \mathbb{C}^3$ and $x \in \mathbb{R}^3$ we want to expand $f_\zeta(x)$ in terms of spherical harmonics with the known expansion

$$\begin{aligned} f_\zeta(\theta, \phi) &= \sum_{l=0}^{\infty} \sum_{m=-l}^l a_{lm} Y_l^m(\theta, \phi) \quad \text{with} \\ a_{lm} &= \int_B f_\zeta(\theta, \phi) [Y_l^m(\theta, \phi)]^* d\sigma \\ &= \int_0^\pi \int_0^{2\pi} f_\zeta(\theta, \phi) [Y_l^m(\theta, \phi)]^* \sin \theta d\theta d\phi \end{aligned}$$

First write f in terms of spherical coordinates

$$f_\zeta(x) = e^{ix \cdot \zeta} = e^{i(x_1 \zeta_1 + x_2 \zeta_2 + x_3 \zeta_3)} = e^{i(\zeta_1 r \sin \theta \cos \phi + \zeta_2 r \sin \theta \sin \phi + \zeta_3 r \cos \theta)} = f_\zeta(\theta, \phi)$$

and then have a closer look at the Y_l^m . By definition

$$Y_l^m(\theta, \phi) = N_l^m P_l^m(\cos \theta) e^{im\phi}$$

where $N_l^m = \sqrt{\frac{(2l+1)(l-m)!}{4\pi(l+m)!}}$ is the normalization factor depending on l, m and P_l^m is an associated Legendre function. The complex conjugate of Y_l^m is given by

$$\begin{aligned} [Y_l^m]^* &= (-1)^m Y_l^{-m} \\ &= (-1)^m N_l^{-m} P_l^{-m}(\cos \theta) e^{-im\phi} \\ &\quad \text{with } P_l^{-m} = (-1)^m \frac{(l-m)!}{(l+m)!} P_l^m \\ &= \sqrt{\frac{(2l+1)(l+m)!}{4\pi(l-m)!}} \frac{(l-m)!}{(l+m)!} P_l^m(\cos \theta) e^{-im\phi} \\ &= \sqrt{\frac{(2l+1)(l-m)!}{4\pi(l+m)!}} P_l^m(\cos \theta) e^{-im\phi} \\ &= N_l^m P_l^m(\cos \theta) e^{-im\phi} \end{aligned}$$

A closer look at the a_{lm} 's shows:

$$\begin{aligned} a_{lm}(\zeta) &= \int_0^{2\pi} \int_0^\pi f_\zeta(\theta, \phi) [Y_l^m(\theta, \phi)]^* \sin \theta d\theta d\phi \\ &= N_l^m \int_0^\pi P_l^m(\cos \theta) \sin \theta \int_0^{2\pi} e^{-im\phi} f_\zeta(\theta, \phi) d\phi d\theta \quad (3.14) \end{aligned}$$

Equation (3.14) can be calculated with numerical integration schemes such as Gaussian quadrature or Simpson's rule. Note that the inner integral is the Fourier transform of $f_\zeta(\theta, \phi)$ in the ϕ direction. To assess the accuracy of the computed a_{lm} 's I compare f_ζ with $\tilde{f}_\zeta(\theta, \phi) = \sum_{l=0}^n \sum_{m=-l}^l a_{lm} Y_l^m(\theta, \phi)$. As expected, as l gets larger the approximation \tilde{f}_ζ gets better. Unfortunately, my straightforward implementation to calculate a_{lm} with numerical integration breaks down for large $|\zeta|$ due to the highly oscillatory nature of the problem. Additionally, the calculation is slow for large l . Therefore a software package called '*S2kit*' is used which gives satisfactory results for l and $|\zeta|$ large. '*S2kit*' is C-code that can be accessed from Matlab. The idea in this software package is to use the Fast Fourier Transform for the inner integral and see the rest as a projection onto the associated Legendre polynomials. To execute that projection they use a three-term recurrence formula for the Associated Legendre functions and then convert the problem into the cosine Fourier space. Detailed information can be found in [25].

In a similar way we can expand a function in terms of $[Y_l^m]^*$, the conjugate of the spherical harmonics. In mathematical terms

$$\begin{aligned}
f_\zeta(\theta, \phi) &= \sum_{l=0}^{\infty} \sum_{m=-l}^l a_{lm}^* [Y_l^m(\theta, \phi)]^* \quad \text{with} \\
a_{lm}^* &= \int_B f_\zeta(\theta, \phi) Y_l^m(\theta, \phi) d\sigma \\
&= (-1)^m \int_B f_\zeta(\theta, \phi) (-1)^m Y_l^m(\theta, \phi) d\sigma \\
&= (-1)^m \int_B f_\zeta(\theta, \phi) [Y_l^{-m}(\theta, \phi)]^* d\sigma \\
&= (-1)^m a_{l(-m)}
\end{aligned}$$

3.2.2 The Fourier Transform and its Discretization

The Fourier transform is a very powerful tool for theory and applications. In this work we can find it in several places. We can find it in the definition of the Faddeev's Green's function, which is defined in terms of the inverse Fourier transform of the function $(\xi^2 + 2\zeta \cdot \xi)^{-1}$, in step 3 where we determine the Schrödinger potential from an approximation of its inverse Fourier transform and in the calculation of the spherical harmonics expansion coefficients.

The definition of the Fourier transform

Before we start any discussion about the Fourier transform (FT) we need a few words about the different definitions of the FT. The difference is the factor 2π which is sometimes used as a coefficient and sometimes it is in the exponent. For example, Nachman uses in [62] the definition

$$\mathcal{F}(g(x))(\xi) = \int_{\mathbb{R}^n} g(x) e^{-ix \cdot \xi} dx.$$

In comparison, Matlab's definition of the Fourier transform is

$$\mathcal{F}(g(x))(\xi) = \int_{\mathbb{R}^n} g(x) e^{-i2\pi x \cdot \xi} dx,$$

and these examples are not the only ones. There are a few more versions. Through a change of variables we can find a relation between the different expressions. If \hat{g}_N denotes the FT of the function g according to Nachman's definition and \hat{g}_M the FT of G according to Matlab's definition we can write

$$\hat{g}_N(\xi) = \hat{g}_M\left(\frac{\xi}{2\pi}\right).$$

That gives us the possibility to leave the theory in Nachman's notation and do the actual calculations with Matlab's expression.

An example of a discretization

One difficulty with the Fourier transform (FT) is the transition to the discrete Fourier transform. Let us use an example to illustrate this. Consider the step function

$$g(x) = \begin{cases} 1 & |x| \leq \frac{1}{2} \\ 0 & \text{otherwise} \end{cases}$$

and its Fourier transform

$$\hat{g}(\alpha) = \int_{\mathbb{R}} g(x)e^{-ix\alpha} dx.$$

A closer look at the integrand $g(x)e^{-ix\alpha}$ reveals that the larger α the more oscillatory is the integrand. That leads to the fact that for large α 's the FT goes to zero due to the cancellation of the positive and negative parts. With small α -values this is not the case. Figure 3.1 demonstrates what

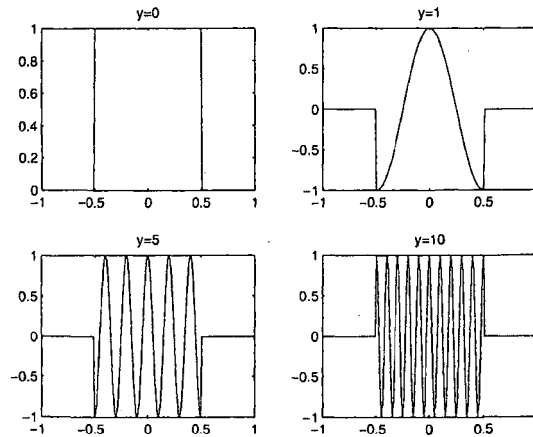


Figure 3.1: The integrand when taking the Fourier transform

the integrand looks like for a few different α 's. Clearly, for $\alpha = 0$ we get $\hat{g}(0) = 1$ whereas for $\alpha = 10$ we get $\hat{g}(10) = \text{sinc}\left(\frac{10}{2}\right) = -.19$. Now consider $\alpha = 10$ and the discretization $x = \frac{k\pi}{5}$ with k any integer. The integrand is $e^{-i\frac{k\pi}{5}10} = e^{-i2\pi k} = 1$. This implies that with this discretization we get $\hat{g}(0) = \hat{g}(10)$. This suggests that the DFT gives a periodic function even though the FT is not.

The Discrete Fourier transform

Is the hypothesis that the DFT gives periodic function right and why is this the case? Corollary 36.6 in [44] says

“Suppose f and F are two generalized functions with $F = \mathcal{F}[f]$.

Then one is periodic if and only if the other is a regular array of delta functions. Moreover, the period of the periodic function and the spacing of the array are reciprocals of each other.”³

In other words, *if we have a discretized or sampled function then the Fourier transform is periodic and the inverse Fourier transform of a discretized function is periodic as well.* In practice we can not have infinitely many discretization points and hence we need some truncation. The periodicity helps us to choose such a truncation since one period gives all the information that is needed. Consider a periodic function $g(x)$ with period P_1 and discretize it with equidistant spacing of Δx . Then the Fourier transform $\hat{g}(\xi) = \mathcal{F}(g)$ is periodic with period $P_2 = \frac{1}{\Delta x}$. Moreover, when we take the inverse Fourier transform of it, we need to get a function of period P_1 which

³A regular array has equidistant spacing.

implies the spacing $\Delta\xi = \frac{1}{P_1}$. This gives a unique number of discretization points, namely $N = \frac{P_1}{\Delta x} = \frac{P_2}{\Delta\xi}$. The conclusion of all this is that if we work with the DFT we have a limited choice of discretization. We can only choose two of the following 5 variables: number of discretization points, spacing Δx , spacing $\Delta\xi$, truncation (or period) P_1 and P_2 . All other variables are uniquely defined by these choices. Another good explanation can be found in the book by E. Oran Brigham [16] in which he has among others a very nice visual explanation.

In practice the discretization depends also on the method of calculation of the DFT. Using a numerical integration scheme such as Simpson's Rule gives more freedom in choosing the discretization, but we still need to be aware of the effect of the periodicity, to avoid introducing artifacts. If we use the Fast Fourier Transform (FFT) we need to be exact as described above for our discretization. The knowledge of the relation between a discretized function and its discretized FT helps in finding the relation $\xi = \frac{x}{N(\Delta x)^2}$ (using Matlab's FT).

3.2.3 Eigenvalues and Eigenfunctions of the DtN Map

For the calculation of the scattering data we need to be able to express the DtN map Λ_γ . In future work this will be the measured data. In this context we express the DtN map in terms of its eigenvalues and eigenfunctions. This section shows that the spherical harmonics are eigenfunctions of the DtN map in the case of spherically symmetric conductivities. Moreover, we derive an expression for the eigenvalues for piecewise constant, spherically symmetric conductivities. A similar expression for the eigenvalues in 2D was derived in [67]. The eigenvalues of piecewise constant conductiv-

ities can be used to approximate the eigenvalues of smooth conductivity distributions which is explained in section 3.2.4.

Proposition 3.2.1. *Given the unit sphere, D and a spherically symmetric conductivity distribution $\gamma(r)$, the spherical harmonics, Y_l^m , are eigenfunctions of the DtN map, Λ_γ .*

Proof. The generalized Laplace equation in spherical coordinates is

$$\begin{aligned} 0 = \nabla \cdot (\gamma \nabla u) &= \frac{1}{r^2} \frac{\partial}{\partial r} \left(r^2 \gamma \frac{\partial u}{\partial r} \right) + \frac{1}{r^2 \sin \theta} \frac{\partial}{\partial \theta} \left(\gamma \sin \theta \frac{\partial u}{\partial \theta} \right) \\ &\quad + \frac{1}{r^2 \sin^2 \theta} \frac{\partial}{\partial \phi} \gamma \frac{\partial u}{\partial \phi} \end{aligned} \quad (3.15)$$

For separation of variables let $u(r, \theta, \phi) = R(r)\Theta(\theta)\Phi(\phi)$, and the equation can be written as

$$0 = \frac{1}{R} \frac{\partial}{\partial r} \left(r^2 \gamma \frac{\partial R}{\partial r} \right) + \frac{1}{\Theta \sin \theta} \frac{\partial}{\partial \theta} \left(\gamma \sin \theta \frac{\partial \Theta}{\partial \theta} \right) + \frac{1}{\Phi \sin^2 \theta} \frac{\partial}{\partial \phi} \gamma \frac{\partial \Phi}{\partial \phi}$$

Using the standard techniques for separation of variables we see that $Y_l^m(\theta, \phi) = \Theta(\theta)\Phi(\phi)$ where $Y_l^m(\theta, \phi)$ are spherical harmonics and the general solution is $u = \sum_{l=0}^{\infty} \sum_{m=-l}^l R_l(r) Y_l^m(\theta, \phi)$. Imposing the Dirichlet data $u|_{\partial D} = Y_l^m(\theta, \phi)$ gives a particular solution with the following DtN map

$$\begin{aligned} \Lambda_\gamma Y_l^m(\theta, \phi) &= \Lambda_\gamma u|_{\partial D} = \Lambda_\gamma u|_{r=1} \\ &= \gamma \left. \frac{\partial R_l(r) Y_l^m(\theta, \phi)}{\partial r} \right|_{r=1} \\ &= \gamma \left. \frac{\partial R_l}{\partial r} \right|_{r=1} Y_l^m(\theta, \phi) \\ &= \lambda_l Y_l^m(\theta, \phi) \end{aligned} \quad (3.16)$$

which completes the proof. \square

Note that λ is independent of m since R_l is independent of m . To get the eigenvalues of the DtN map of piecewise continuous and spherically symmetric conductivities we consider the unit sphere in \mathbb{R}^3 with $(N-1)$ spherical inclusions centered at the origin with radius $0 < r_1 < \dots < r_{N-1} < 1$. Moreover, let $r_0 = 0$ and $r_N = 1$. The conductivity is assumed to be constant within each inclusion i.e., $\gamma(r) = \gamma_j$ for $r_{j-1} \leq r \leq r_j, j = 1, \dots, N$. We would like to construct the function u_{lm} that solves $\nabla \cdot \gamma \nabla u_{lm} = 0$ with $u_{lm}|_{r=1} = Y_l^m$ and γ as described above. If γ is constant in a spherically symmetric domain, then we have $\Delta u = 0$ and separation of variables gives the solution

$$u(r, \theta, \phi) = \sum_l \sum_m (A(l)r^l + B(l)r^{-(l+1)}) Y_l^m(\theta, \phi) \quad (3.17)$$

where a, b are constants determined by boundary conditions. For the case with inclusions and constant conductivity within each inclusion, we have $u_{lm} = v_l(r)Y_l^m(\theta, \phi)$ with $v_l(r) = A_j r^l + B_j r^{-(l+1)}$ for $r_{j-1} \leq r < r_j, j = 1, \dots, N$. Note that the dependence of A and B on l is not explicitly indicated. For physically feasible solutions we need to set $B_1 = 0$ (otherwise we have a blow up at zero). All other coefficients A_j and B_j are determined by the 'boundary' conditions on the inclusions, by matching Dirichlet and Neumann conditions at each r_j for $j = 1, \dots, N - 1$. The Dirichlet conditions at r_j for $j = 1, \dots, N - 1$ are defined by

$$\begin{aligned} A_j r_j^l + B_j r_j^{-(l+1)} &= A_{j+1} r_j^l + B_{j+1} r_j^{-(l+1)} \\ A_j + B_j w_j &= A_{j+1} + B_{j+1} w_j \end{aligned} \quad (3.18)$$

with $w_j = r_j^{-(2l+1)}$ and the matching Neumann conditions at r_j for $j = 1, \dots, N - 1$ are

$$\begin{aligned} \gamma_j (l A_j r_j^{l-1} - (l+1) B_j r_j^{-(l+2)}) &= \gamma_{j+1} (l A_{j+1} r_j^{l-1} - (l+1) B_{j+1} r_j^{-(l+2)}) \\ \gamma_j (A_j - \beta B_j w_j) &= \gamma_{j+1} (A_{j+1} - \beta B_{j+1} w_j) \end{aligned} \quad (3.19)$$

with $\beta = (l+1)/l$ and w_j as above. Last but not least we have the Dirichlet condition at r_N given by

$$\begin{aligned}
Y_l^m(\theta, \phi) &= u_{lm}|_{r_N} = v_l(r_N)Y_l^m(\theta, \phi) \\
&= (A_N r_N^l + B_N r_N^{-(l+1)})Y_l^m(\theta, \phi) \\
1 &= A_N r_N^l + B_N r_N^{-(l+1)} \quad \text{with } r_N = 1 \\
1 &= A_N + B_N
\end{aligned} \tag{3.20}$$

Once we have constructed u_{lm} we express the eigenvalues of the DtN with the help of equation (3.16),

$$\begin{aligned}
\lambda_l &= \gamma \left. \frac{\partial R}{\partial \nu} \right|_{\partial D} \\
&= \gamma \left. \frac{\partial v_{lm}}{\partial r} \right|_{\partial D} \\
&= \gamma_N (l A_N r_N^{l-1} - (l+1) B_N r_N^{-(l+2)}) \\
&\quad \text{and with } r_N = 1 \text{ and } \gamma_N = 1 \\
\lambda_l &= l A_N - (l+1) B_N
\end{aligned}$$

From equation (3.20)

$$\begin{aligned}
\lambda_l &= l(1 - B_N) - (l+1) B_N \\
&= l - (2l+1) B_N
\end{aligned} \tag{3.21}$$

This leaves us with the problem of finding B_N . First we express A_N in terms of B_N which is done recursively, see Proposition 3.2.2. Then use equation (3.20) to find an expression for B_N which can be used in (3.21).

Lemma 3.2.2. *Suppose we have $N-1$ inclusions in the unit sphere as described above. Then $A_j = B_j C_{j-1}$ for $j = 2, \dots, N$ where C_j is recursively defined by $C_j = w_j \frac{\beta \gamma_{j+1} \rho_j + \gamma_j}{\gamma_{j+1} \rho_j - \gamma_j}$ with $\rho_1 = 1$, $\rho_j = \frac{C_{j-1} + w_j}{C_{j-1} - \beta w_j}$, $\beta = \frac{l+1}{l}$ and $w_j = r_j^{-(2l+1)}$.*

Proof. We will prove the Proposition by induction. The boundary conditions on the first inclusion, see equation (3.18) and (3.19), are given by

$$\begin{aligned} A_1 &= A_2 + B_2 w_1 \\ \gamma_1 A_1 &= \gamma_2 (A_2 - \beta B_2 w_1) \end{aligned}$$

which can be solved for A_2 in term of B_2

$$\begin{aligned} \gamma_1(A_2 + B_2 w_1) &= \gamma_2 (A_2 - \beta B_2 w_1) \\ A_2(\gamma_2 - \gamma_1) &= B_2 w_1(\beta \gamma_2 + \gamma_1) \\ A_2 &= B_2 C_1 \end{aligned}$$

Now suppose $A_j = B_j C_{j-1}$. We need to show that $A_{j+1} = B_{j+1} C_j$. We will use the boundary condition on the j th inclusion given by equation (3.18) and (3.19). First we solve for B_j in terms of A_{j+1} and B_{j+1} from the Dirichlet condition at r_j

$$\begin{aligned} A_j + B_j w_j &= A_{j+1} + B_{j+1} w_j \\ B_j(C_{j-1} + w_j) &= A_{j+1} + B_{j+1} w_j \\ B_j &= \frac{A_{j+1} + B_{j+1} w_j}{C_{j-1} + w_j} \end{aligned}$$

and then find A_{j+1} using the Neumann condition at r_j

$$\begin{aligned} \gamma_j(A_j - \beta B_j w_j) &= \gamma_{j+1}(A_{j+1} - \beta B_{j+1} w_j) \\ \gamma_j B_j(C_{j-1} - \beta w_j) &= \gamma_{j+1}(A_{j+1} - \beta B_{j+1} w_j) \\ \gamma_j \frac{A_{j+1} + B_{j+1} w_j}{C_{j-1} + w_j} (C_{j-1} - \beta w_j) &= \gamma_{j+1}(A_{j+1} - \beta B_{j+1} w_j) \\ \gamma_j(A_{j+1} + B_{j+1} w_j) &= \gamma_{j+1}(A_{j+1} - \beta B_{j+1} w_j) \rho_j \\ A_{j+1} &= B_{j+1} w_j \frac{\beta \gamma_{j+1} \rho_j + \gamma_j}{\gamma_{j+1} \rho_j - \gamma_j} \\ &= B_{j+1} C_j \end{aligned}$$

□

Once we have A_N we also have $B_N = 1 - A_N$ which gives the eigenvalues.

Theorem 3.2.3. *Given the unit sphere with $N - 1$ inclusions centered at the origin with radius $0 < r_1 < r_2 < \dots < r_{N-1} < 1$ and constant conductivity within each inclusion, given by γ_j , $j = 1, \dots, N - 1$ and letting $r_0 = 0$, $r_N = 1$ and $\gamma_N = 1$ then the eigenvalues of Λ_γ are given by*

$$\lambda_l = l - \frac{2l + 1}{1 + C_{N-1}}$$

where $C_j = w_j \frac{\beta\gamma_{j+1}\rho_j + \gamma_j}{\gamma_{j+1}\rho_j - \gamma_j}$ with $\rho_1 = 1$, $\rho_j = \frac{C_{j-1} + w_j}{C_{j-1} - \beta w_j}$, $\beta = \frac{l+1}{l}$ and $w_j = r_j^{-(2l+1)}$.

Proof. From the Proposition 3.2.2 we have $A_N = B_N C_{N-1}$. Together with equation (3.20) we get $B_N = (C_{N-1} - 1)^{-1}$ which we substitute into equation (3.21). \square

Lemma 3.2.4. *The eigenvalue of the DtN map associated with $Y_0^0(\theta, \phi)$ is zero ($\lambda_0 = 0$).*

Proof. The spherical harmonic Y_0^0 is a constant. The min-max principle implies that the solution to the Laplace equation with constant boundary value is that constant. So with no inclusion (constant conductivity) and boundary condition $u|_{\partial D} = Y_0^0$ we have $u = Y_0^0$. If we have inclusions then the matching Dirichlet and Neuman conditions on the boundary are

$$\begin{aligned} A_j(0) + B_j(0)r_j^{-1} &= A_{j+1}(0) + B_{j+1}(0)r_{j+1}^{-1} \\ -\gamma_j B_j r_j^{-2} &= -\gamma_{j+1} B_{j+1} r_{j+1}^{-2} \end{aligned}$$

The last equation shows that that all B_j 's must be zero since $B_1 = 0$. So for the region $r_{N-1} \leq |x| \leq r_N$ the solution can be written as $u = A_N Y_0^0$. So with and without inclusion we have a constant function whose derivative is zero and hence $\Lambda Y_0^0 = \frac{\partial u}{\partial r}|_{\partial D} = 0$. \square

Corollary 3.2.5. *The eigenvalues of the DtN map for a homogeneous conductivity distribution are given by $\lambda_l = l$.*

Proof. The solution to the Laplace equation is given by (3.17) with $b = 0$. Imposing the Dirichlet condition $Y_l^m(\theta, \phi)$ we get $u(r, \theta, \phi) = r^l Y_l^m(\theta, \phi)$. From equation (3.21) we can see that $\lambda_l = l$. \square

Let λ_l be the eigenvalues of the DtN map of a given (non constant) conductivity distribution. Then the eigenvalues of $\Lambda_\gamma - \Lambda_1$ are $\lambda_l - l$. The difference goes to zero as l gets large. That helps in the calculation of the scattering data since we only use the first few eigenvalues.

There are a few more interesting facts that we can deduce from the eigenvalues. If we have one inclusion then the eigenvalues approach l as the radius of the inclusion goes to zero. Similarly, the closer the magnitude is to one the less the eigenvalues differ from l . The conclusion is that it is easier to detect inclusions that are bigger and have a larger change in conductivity.

3.2.4 Eigenvalues of a Smooth Conductivity Distribution

So far we considered the eigenvalues of conductivity distributions that were step functions which are not smooth. The problem in this context is that we require $\gamma \in C^{1,1}$. So how can we find the eigenvalues of a smooth conductivity? From [69] we know that if $\gamma_L(r) \leq \gamma_U(r)$ for all r then $\lambda_l^L \leq \lambda_l^U$. This gives a means for finding lower and upper bounds on the eigenvalues of a smooth function by finding the eigenvalues of piecewise constant function, γ_L and γ_U that satisfy $\gamma_L(r) \leq \gamma(r) \leq \gamma_U(r)$.

To demonstrate the procedure and the results I use the conductivity distribution⁴

$$\gamma(r) = (\alpha\Psi(r) + 1)^2 \quad (3.22)$$

$$\Psi(r) = \begin{cases} e^{-\frac{r^2}{(r^2-d^2)\gamma^2}} & \text{for } -d < r < d \\ 0 & \text{otherwise} \end{cases} \quad (3.23)$$

and with $d = .9$ and $\alpha = 1$. The idea of step functions as lower and upper bound is depicted in figure 3.2. We see that the approximation of the

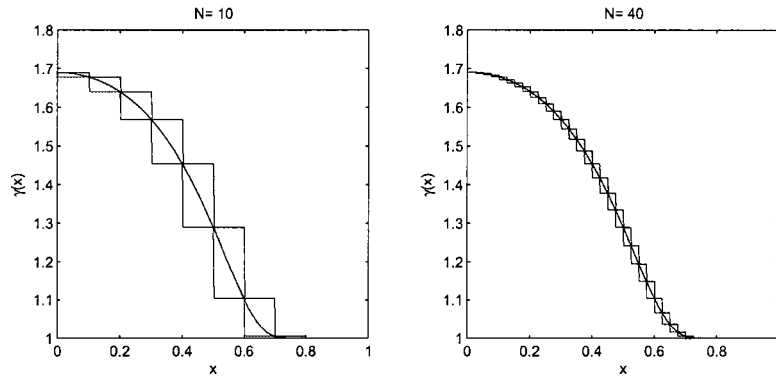


Figure 3.2: Approximation of a smooth curve with step functions. On the left a coarse approximation with $N = 10$ steps and on the right a finer approximation with $N = 40$ steps

smooth curve is better the finer steps or the more steps are used. Table 3.1 shows the difference of the approximation of the eigenvalues with the upper and lower bound step functions with different numbers of steps, $N = 50$, $N = 500$ and $N = 5000$. Since we know that the actual eigenvalues are bounded by the eigenvalues of the lower and upper step functions, a small difference in the eigenvalues of the step function implies a good approximation to the eigenvalues of the smooth function. As it is seen in the table the

⁴See section 3.5.1 for more details about this conductivity distribution.

Difference of eigenvalues

l	$N = 50$	$N = 500$	$N = 5000$
1	0.02728701	0.00272747	0.00027274
2	0.02446984	0.00244352	0.00024434
3	0.01700983	0.00169604	0.00016959
4	0.01065320	0.00106004	0.00010599
5	0.00631207	0.00062645	0.00006264
6	0.00362077	0.00035823	0.00003581
7	0.00203660	0.00020077	0.00002007
8	0.00113190	0.00011113	0.00001111
9	0.00062460	0.00006104	0.00000610
10	0.00034328	0.00003338	0.00000333
11	0.00018831	0.00001821	0.00000182
12	0.00010326	0.00000992	0.00000099
13	0.00005665	0.00000541	0.00000054
14	0.00003112	0.00000295	0.00000029

Table 3.1: The table displays the difference of the upper and lower bound of the first 14 eigenvalues of the DtN of the example given in (3.23). With increased number of steps, N , the bounds are getting better.

difference of the eigenvalues gets smaller with an increased number of steps. Hence the approximation of the eigenvalues of a smooth function increases with the refinement of the step function approximation.

In practice the eigenvalues were calculated by taking the average of the lower and the upper bound and taking $N = 500$. As can be seen in section 3.3 we will need the difference $\lambda_l - l$ with $l = 0, 1, 2, \dots$. Table 3.2 presents the first 14 eigenvalues of the function given by (3.23) and the difference $\lambda_l - l$.

3.2.5 Choosing ξ and ζ

When we expressed the scattering data in terms of a boundary integral, we introduced the condition that

$$(\xi + \zeta)^2 = 0 \tag{3.24}$$

Eigenvalues

l	λ_l	$\lambda_l - l$
1	1.157894736	0.157894736
2	2.070422535	0.070422535
3	3.025331724	0.025331724
4	4.008279668	0.008279668
5	5.002558258	0.002558258
6	6.000761763	0.000761763
7	7.000220992	0.000220992
8	8.000062884	0.000062884
9	9.000017630	0.000017630
10	10.000004884	0.000004884
11	11.000001340	0.000001340
12	12.000000364	0.000000364
13	13.000000098	0.000000098
14	14.000000026	0.000000026

Table 3.2: Calculated eigenvalues λ_l and the difference $\lambda_l - l$

where $\xi \in \mathbb{R}^n$ and $\zeta \in \mathbb{C}^n$. From the exponentially growing solution $\psi(x, \zeta)$ we also have

$$\zeta^2 = 0. \tag{3.25}$$

Let $\zeta = \zeta_R + i\zeta_I$. Then (3.25) translates into $\zeta^2 = \zeta_R^2 - \zeta_I^2 + 2i\zeta_R \cdot \zeta_I = 0$ which gives

$$\zeta_R \perp \zeta_I \tag{3.26}$$

$$|\zeta_I| = |\zeta_R| \tag{3.27}$$

and (3.24) is equivalent to $\xi^2 + 2\zeta_R \cdot \xi + i2\zeta_I \cdot \xi = 0$ which leads to

$$\zeta_I \perp \xi \tag{3.28}$$

and

$$\begin{aligned} \xi^2 &= -2\zeta_R \cdot \xi \\ |\xi||\xi| &= -2|\zeta_R||\xi| \cos \alpha \\ |\xi| &= -|\zeta_R| \cos \alpha \end{aligned} \tag{3.29}$$

where α is the angle between ξ and ζ . Conditions (3.26) and (3.28) say that ξ and ζ_R lay in the plane perpendicular to ζ_I and equation (3.29) gives the angle between ξ and ζ . Note that $|\xi|$ must be smaller than $|\zeta_R|$.

Given a ξ we want to find a ζ with a certain magnitude k . The fact that $|\zeta|^2 = \zeta \cdot \bar{\zeta} = |\zeta_R|^2 + |\zeta_I|^2$ and condition (3.27) give that

$$k^2 = 2|\zeta_R|^2 = 2|\zeta_I|^2 \quad \text{or} \quad |\zeta_R| = |\zeta_I| = \frac{k}{\sqrt{2}}$$

So the magnitude of ζ_R and ζ_I are uniquely determined. The direction is not unique. Condition (3.28) says that ζ_I is in the null space of ξ . In practice we choose a vector from that null space with the magnitude $k/\sqrt{2}$ and call it ζ_I . Then we rotate ξ in the plane perpendicular to ζ_I by the angle α to get the direction of ζ_R .

3.3 Implementation of t^{exp} for Spherically Symmetric Conductivities

In this section we derive an equation to calculate the approximation $t^{exp}(\xi, \zeta)$ to the scattering data in the case of a spherically symmetric conductivity distribution. First we expand $e^{ix \cdot \zeta}$ in terms of spherical harmonics as described in section 3.2.1 and $e^{-ix \cdot (\xi + \zeta)}$ in terms of the spherical harmonics conjugates. That leads to

$$\begin{aligned} e^{-ix \cdot (\xi + \zeta)} &= \sum_{l=0}^{\infty} \sum_{m=-l}^{m=l} a_{lm}^*(\xi, \zeta) [Y_l^m(\theta, \phi)]^* \\ e^{ix \cdot \zeta} &= \sum_{k=0}^{\infty} \sum_{n=-k}^{n=k} b_{kn}(\zeta) Y_k^n(\theta, \phi) \end{aligned}$$

Next we use these expansions in equation (3.10) to get

$$\begin{aligned} t^{exp}(\xi, \zeta) &= \int_{\partial D} \sum_{l,m} a_{lm}^*(\xi, \zeta) [Y_l^m(\theta, \phi)]^* (\Lambda_q - \Lambda_0) \sum_{k,n} b_{kn}(\zeta) Y_k^n(\theta, \phi) d\sigma \\ &= \sum_{l,m} \sum_{k,n} a_{lm}^*(\xi, \zeta) b_{kn}(\zeta) \int_{\partial D} [Y_l^m(\theta, \phi)]^* (\Lambda_q - \Lambda_0) Y_k^n(\theta, \phi) d\sigma \end{aligned}$$

Using the result that the spherical harmonics are eigenfunctions of the DtN map from section 3.2.3 leads to

$$\begin{aligned}
t^{exp}(\xi, \zeta) &= \sum_{l,m,k,n} a_{lm}^*(\xi, \zeta) b_{kn}(\xi) \int_{\partial D} [Y_l^m(\theta, \phi)]^* (\Lambda_q - \Lambda_0) Y_k^n(\theta, \phi) d\sigma \\
&= \sum_{l,m,k,n} a_{lm}^*(\xi, \zeta) b_{kn}(\zeta) \int_{\partial D} [Y_l^m(\theta, \phi)]^* (\lambda_k - k) Y_k^n(\theta, \phi) d\sigma \\
&= \sum_{l,m,k,n} a_{lm}^*(\xi, \zeta) b_{kn}(\zeta) (\lambda_k - k) \int_{\partial D} [Y_l^m(\theta, \phi)]^* Y_k^n(\theta, \phi) d\sigma \\
&= \sum_{l,m} a_{lm}^*(\xi, \zeta) b_{lm}(\zeta) (\lambda_l - l) \tag{3.30}
\end{aligned}$$

The last equality comes from the orthonormality of the spherical harmonics. Equation (3.30) can be easily calculated if the coefficients a_{lm}^* and b_{lm} are available.

3.3.1 Symmetry

In this section we investigate some properties of spherically symmetric functions and the scattering transform. We start with the Laplace equation in spherical coordinates which is given by equation (3.15) with $\gamma = 1$. Given a spherically symmetric function $u(r)$ the Laplace equation reduces to

$$\Delta u(r) = \frac{\partial}{\partial r} r^2 \frac{\partial u(r)}{\partial r}$$

which is independent of θ and ϕ and therefore the Laplace operator preserves the symmetry. If we consider a spherically symmetric conductivity distribution $\gamma(r)$ then the Schrödinger potential $q(r) = \frac{\Delta \sqrt{\gamma(r)}}{\sqrt{\gamma(r)}}$ is spherically symmetric as well. This in turn implies $\hat{q}(x)$ is spherically symmetric which can be shown using the the definition of the Fourier transform and a

orthogonal matrix R .

$$\begin{aligned}
\hat{q}(\xi) &= \int_{\mathbb{R}^3} q(x) e^{i x \cdot \xi} dx \\
&\quad \text{let } x = R\bar{x} \\
&= \int q(R\bar{x}) e^{i(R\bar{x}) \cdot \xi} d\bar{x} \\
&= \int q(\bar{x}) e^{i\bar{x} \cdot (R\xi)} d\bar{x} \\
&= \hat{q}(R\xi)
\end{aligned}$$

In other words $\hat{q}(\xi) = \hat{q}(|\xi|) = \lim_{|\zeta| \rightarrow \infty} t(|\xi|, \zeta)$. Cornean et. al. showed in [24] that $t(R\xi, \zeta) = t(\xi, R^T\zeta)$ if R is an orthogonal matrix. All together this gives

$$\lim_{|\zeta| \rightarrow \infty} t(\xi, \zeta) = \lim_{|\zeta| \rightarrow \infty} t(R\xi, \zeta) = \lim_{|\zeta| \rightarrow \infty} t(\xi, R^T\zeta)$$

This implies that $\lim_{|\zeta| \rightarrow \infty} t(\xi, \zeta)$ is independent of the direction of ξ and ζ .

Additionally the spherical symmetry allows us to show results as one dimensional rays. All plots in the following sections show only a one dimensional ray of the 3 dimensional spherically symmetric functions. Another advantage of the symmetry is that we can reduce some of the calculations from three dimensions to one dimension which saves computation time and memory resources.

3.4 Implementation Details for Obtaining the Conductivity Distribution γ .

In section 3.1.4 we showed that the solution of the differential equation $q = \gamma^{-\frac{1}{2}} \Delta \gamma^{\frac{1}{2}}$ can be reduced to the solution of the integral equation

$$\sqrt{\gamma(x)} = \frac{1}{a} - \frac{1}{4\pi} \int_D \frac{1}{|x-y|} - \frac{a}{|x||x^*-y|} q(y) \sqrt{\gamma(y)} dy.$$

This section describes in more details how this integral equation is solved. To simplify notation let $\sqrt{\gamma} = u$ and we can write

$$Au + u = (A + I)u = \frac{1}{a} \quad (3.31)$$

where $Au = \frac{1}{4\pi} \int_D \left(\frac{1}{|x-y|} - \frac{a}{|x||x^*-y|} \right) (q(y)u(y)) dy$ and I is the identity operator. If we discretize this equation we get a system of linear equations. We chose to use an iterative method to solve this system and a GMRES ('generalized minimal residual') algorithm seem to be a good choice since the system is sparse. More specifically we use Matlab's gmres routine. For this we need a Matlab routine that calculates $(A - I)u$. Even though Au could be calculated, it is computationally expensive since it is a triple integral. For our use we can reduce Au as follows. With x , x^* and y in spherical coordinates as in section 3.1.4 we have

$$\begin{aligned} \frac{1}{\frac{|x-y|}{a}} &= \frac{1}{(r^2 + r'^2 - 2rr'(\sin \theta \sin \theta' \cos(\phi - \phi') + \cos \theta \cos \theta'))^{1/2}} \\ \frac{1}{|x||x^* - y|} &= \frac{1}{r \left(\frac{a^4}{r^2} + r'^2 - 2\frac{a^2 r'}{r} (\cos(\phi - \phi') \sin \theta \sin \theta' + \cos \theta \cos \theta') \right)^{1/2}} \\ &= \frac{1}{\left(a^2 + \frac{r^2 r'^2}{a^2} - 2r'r(\cos(\phi - \phi') \sin \theta \sin \theta' + \cos \theta \cos \theta') \right)^{1/2}} \end{aligned}$$

Since we work with spherically symmetric conductivities we know that u is symmetric and therefore Au must be spherically symmetric too. Therefore we can reduce the problem to calculate $Au(|x|)$. For this we chose x to lie

on the the z-axis, or in other words we choose $\theta = 0$ and $\phi = 0$, which gives

$$\begin{aligned}
& Au(r, 0, 0) \\
&= \frac{1}{4\pi} \int_0^a \int_0^\pi \int_0^{2\pi} \left(\frac{1}{(r^2 + r'^2 - 2rr' \cos \theta')^{1/2}} \right. \\
&\quad \left. - \frac{1}{(a^2 + \frac{r^2 r'^2}{a^2} - 2rr' \cos \theta')^{1/2}} \right) q(r)u(r)r'^2 \sin \theta' d\phi' d\theta' dr' \\
&= \frac{2\pi}{4\pi} \int_0^a \int_0^\pi \left(\frac{1}{(r^2 + r'^2 - 2rr' \cos \theta')^{1/2}} \right. \\
&\quad \left. - \frac{1}{(a^2 + \frac{r^2 r'^2}{a^2} - 2rr' \cos \theta')^{1/2}} \right) q(r)u(r)r'^2 \sin \theta' d\theta' dr' \\
&\quad \text{use } u_1 = r^2 + r'^2 - 2rr' \cos \theta' \\
&\quad \text{and } u_2 = a^2 + \frac{r^2 r'^2}{a^2} - 2rr' \cos \theta' \\
&= \frac{1}{2} \int_0^a \left(\int_{u_1(0)}^{u_1(\pi)} \frac{r'}{2ru_1^{1/2}} du_1 - \int_{u_2(0)}^{u_2(\pi)} \frac{r'}{2ru_2^{1/2}} du_2 \right) q(r)u(r)dr' \\
&= \frac{1}{2} \int_0^a \frac{r'}{r} \left(\left(u^{1/2} \Big|_{(r-r')^2}^{(r+r')^2} \right) - \left(u^{1/2} \Big|_{(a-\frac{rr'}{a})^2}^{(a+\frac{rr'}{a})^2} \right) \right) q(r)u(r)dr' \\
&= \frac{1}{2} \int_0^a \frac{r'}{r} \left(|r+r'| - |r-r'| - \left| a + \frac{rr'}{a} \right| + \left| a - \frac{rr'}{a} \right| \right) q(r)u(r)dr' \\
&= \frac{1}{2} \int_0^a \frac{r'}{r} \left(r+r' - |r-r'| - a - \frac{rr'}{a} + a - \frac{rr'}{a} \right) q(r)u(r)dr' \\
&= \frac{1}{2} \int_0^r \frac{r'}{r} \left(2r' - \frac{2rr'}{a} \right) q(r)u(r)dr' + \frac{1}{2} \int_r^a \frac{r'}{r} \left(2r - \frac{2rr'}{a} \right) q(r)u(r)dr' \\
&= \frac{1}{r} \int_0^r r'^2 \left(1 - \frac{r}{a} \right) q(r)u(r)dr' + \int_r^a r' \left(1 - \frac{r'}{a} \right) q(r)u(r)dr' \\
&= \left(\frac{1}{r} - \frac{1}{a} \right) \int_0^r r'^2 q(r)u(r)dr' + \int_r^a \left(r' - \frac{r'^2}{a} \right) q(r)u(r)dr'
\end{aligned}$$

This equation reduces the triple integrals into two single integrals which speeds up the calculation in the gmres routine significantly.

To calculate the two integrals I use the Simpson's rule. When r is close to zero or close to a we have only very few sample points in one of the integrals which causes inaccuracies with the Simpson's rule. To avoid this I included some interpolation routines.

Using the Fast Fourier transform (FFT) could be another way of calculating Au . The idea is that we can write $Au = \int_D G(x-y)q(y)u(y)dy = G * (qu)$. Taking the Fourier transform we just get a multiplication of $\mathcal{F}(G)\mathcal{F}(qu)$ and with the inverse FFT we get Au .

3.5 Results

3.5.1 The Example

As an example we consider a sphere of radius R as our domain. For convenience we assume that $R = 1$. The conductivity distribution under consideration is smooth and spherically symmetric and given by

$$\gamma(r) = (\alpha\Psi(r) + 1)^2 \quad (3.32)$$

$$\Psi(r) = \begin{cases} e^{-\frac{r^2}{(r^2-d^2)^2}} & \text{for } -d < r < d \\ 0 & \text{otherwise} \end{cases} \quad (3.33)$$

Note that Ψ has compact support which is regulated by the parameter $0 < d \leq 1$. The larger d the larger the support of Ψ . The compact support of Ψ assures that $\gamma \equiv 1$ close to the boundary. The second parameter α regulates the amplitude of γ . The largest amplitude is at $r = 0$ with $(\alpha + 1)^2$ as amplitude. For example when $\alpha = 1$, the maximal amplitude is $(1 + 1)^2 = 4$. A similar function was used in the two dimensional setting, see [67]. For better understanding figure 3.3 shows different conductivity distributions corresponding to different values of d and α .

3.5.2 The Scattering Data

As scattering data we use $t^{exp}(\xi, \zeta)$ as described in section 3.3. Note that this is an approximation to the scattering data but so far it is the only way to calculate the scattering data without using the conductivity

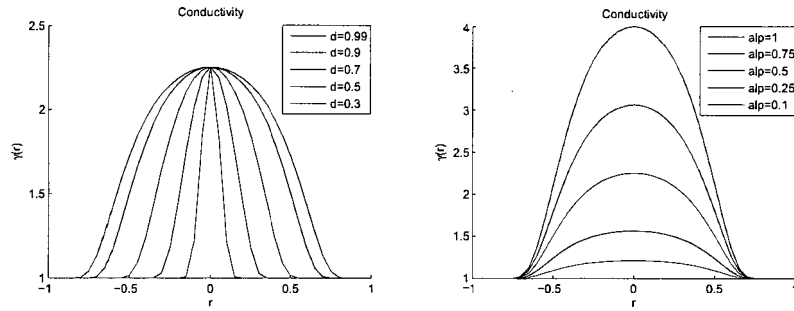


Figure 3.3: The first plot shows the change in $\gamma(r)$ when the parameter d varies and the second plot shows how $\gamma(r)$ varies with α .

distribution explicitly. The parameters that influence t^{exp} are the number of eigenvalues and the truncation of the spherical harmonic expansion. As can be seen in table 3.1, the difference $\Lambda_\gamma - \Lambda_0$ goes relatively quickly to zero for the given conductivity distribution. Hence the largest influence comes from the first eigenvalues. In the following calculations we use the first 30 eigenvalues. The truncation of the spherical harmonics depends on the functions $e^{-ix \cdot (\xi + \zeta)}$ and $e^{ix \cdot \zeta}$. In the reconstructions we chose to truncate at $l = 30$ which means we use the first 900 spherical harmonics. It turns out that t^{exp} becomes numerically unstable for ζ large, and large here means about $|\zeta| = 30$. A similar effect was observed for 2 dimensional data, see [67, 60]. Moreover, t^{exp} is real and independent of ζ . Hence $t^{exp}(\xi, \zeta) = t^{exp}(\xi) = \lim_{|\zeta| \rightarrow \infty} t^{exp} \xi = \hat{q}^{exp}(\xi)$.

Besides using t^{exp} the scattering data can be calculated when the conductivity distribution $\gamma(x)$ is known and smooth so that the Schrödinger potential $q(x)$ can be determined via the integral equation (3.4). Kim Knudsen⁵ realized an implementation of this integral equation. We refer to this

⁵Department of Mathematics, Technical University of Denmark, Kongens Lyngby, Denmark

data as t^{LS} since it involves the solution of the Lippman-Schwinger equation (3.3). The calculation of $t^{LS}(\xi, \zeta)$ is numerically stable for large $|\zeta|$'s but oscillates slightly. These oscillations are so small that they are negligible for our purpose or in other words: as long as we choose $|\zeta|$ large enough we get the same result for q and hence for the reconstruction of the conductivity distribution γ . More specifically we chose $|\zeta| = 50$.

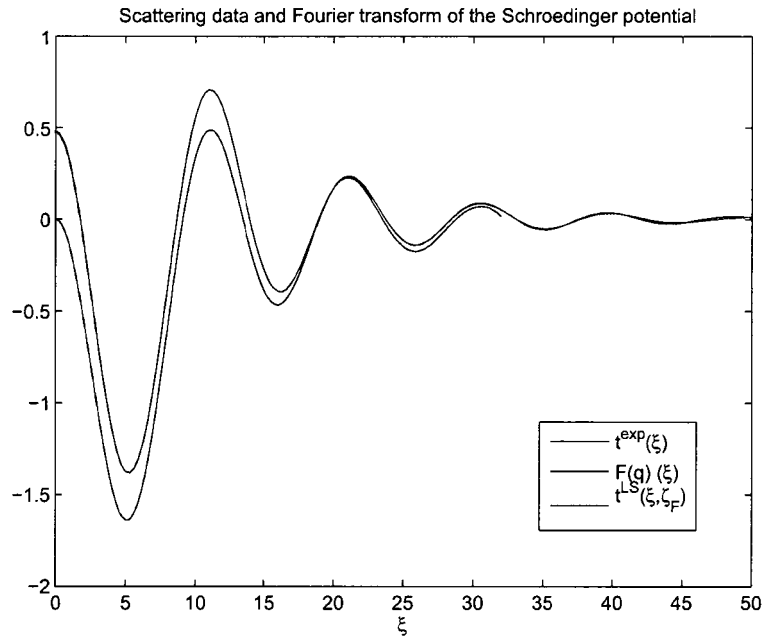


Figure 3.4: Scattering data t^{exp} , t^{LS} for fixed ζ and Fourier transform of the Schrödinger potential with the parameter $d = .9$ and $\alpha = .3$

As a benchmark we use the Fourier transform of the Schrödinger potential which we get from the known conductivity distribution by equation (3.12). This was done with Simpson's rule. Gaussian quadrature is not a good choice. The discretization points for Gaussian quadrature are clustered near the endpoints but q has compact support. Therefore most of

the discretization points have the function values zero which does not contribute to the integrable. The fast Fourier transform (FFT) would be a natural choice but is restricted in the choices of discretization points, see section 3.2.2.

A plot of $t^{exp}(\xi)$, $t^{LS}(\xi, \zeta_F)$ ⁶ and the Fourier transform of the Schrödinger potential, $\hat{q}(\xi)$ is displayed in figure 3.4. The difference in $\hat{q}(\xi)$ and $t^{LS}(\xi, \zeta_F)$ is so small that it is hard to distinguish between the two curves. For $t^{exp}(\xi)$ I used $0 \leq |\xi| \leq 32$ since the calculation gets numerically unstable and blows up for $|\xi| > 32$. We observe good agreement of all 3 curve for $|\xi|$ away from 0. Close to $|\xi| = 0$ the approximation t^{exp} differs from the other values. Since this causes problems we need to investigate this more deeply.

3.5.3 An Investigation of $t^{exp}(0)$

In the last section we saw that $t^{exp}(\xi)$ and $\hat{q}(\xi)$ differ close to $|\xi| = 0$. An investigation needs to consist of two parts. One part is a look into the theory which could include rewriting the expression t^{exp} in a way that is more accessible and/or searching for a bound of $|t^{exp}(0) - t(0, \zeta)|$. The other part is an in depth test of the implemented routines.

⁶ ζ_F means that ζ is fixed

Test of implemented routines

To test my code, especially the expansion into spherical harmonics, I conducted several tests. We will use the following notation:

$$\begin{aligned}
 e^{-ix \cdot (\xi + \zeta)} &= \sum_{l,m} a_{lm} Y_l^m \\
 e^{ix \cdot \zeta} &= \sum_{l,m} b_{lm} Y_l^m \\
 e^{-ix \cdot \zeta} &= \sum_{l,m} b_{lm}^- Y_l^m \\
 e^{ix \cdot \zeta} &= \sum_{l,m} b_{lm}^* [Y_l^m]^*
 \end{aligned}$$

More generally, a minus sign as a superscript of the coefficients means the exponent in the function has the opposite sign and if we expand in terms of the conjugates of the spherical harmonics we write * as a superscript.

The **first test** is the check to see whether the sum of the coefficients multiplied with the spherical harmonics add up to the function itself, mathematically

$$e^{ix \cdot \zeta} = \sum_{l=0}^k \sum_{m=-l}^l b_{lm} Y_l^m.$$

For $k = 30$ and $|\zeta| < 5$ the difference is of order 10^{-13} . The larger the magnitude of ζ the larger we need to choose k . But the expansion works fine.

A **second test** addresses the multiplication of two functions that are expanded in spherical harmonics, more precisely

$$1 = e^{ix \cdot \zeta} e^{-ix \cdot \zeta} = \left(\sum_{l,m} b_{lm} Y_l^m \right) \left(\sum_{k,n} b_{kn}^- Y_k^n \right).$$

The error for this calculation is of order 10^{-13} using the truncation $l, k = 30$ and $|\zeta| \leq 5$.

As a **third test** I consider the integral

$$\int_{\partial D} e^{-ix \cdot \xi} = \int_{\partial D} e^{-ix \cdot (\xi + \zeta)} e^{ix \cdot \zeta}$$

with ∂D the sphere of radius 1. We can calculate the first part analytically

if we use $\xi = k\langle 0, 0, 1 \rangle$,

$$\begin{aligned} \int_{|x|=1} e^{-ix \cdot \xi} dx &= \int_0^\pi \int_0^{2\pi} e^{-i \cos \theta k} \sin \theta d\phi d\theta \\ &= 2\pi \int_0^\pi e^{-i \cos \theta k} \sin \theta d\theta \\ &= \frac{2\pi}{-ia} (e^{-ik} - e^{ik}) \\ &= 4\pi \text{sinc}(k) \end{aligned}$$

The other representation of the integral can be calculated with the spherical harmonic expansions as follows

$$\begin{aligned} \int_{|x|=1} e^{-ix \cdot (\xi + \zeta)} e^{ix \cdot \zeta} dx &= \int_0^\pi \int_0^{2\pi} \sum_{l,m} a_{lm}^* (Y_l^m)^* \sum_{k,n} b_{kn} Y_k^n \sin \theta d\theta d\phi \\ &= \sum_{l,m} \sum_{k,n} a_{lm}^* b_{kn} \int_0^\pi \int_0^{2\pi} (Y_l^m)^* Y_k^n \sin \theta d\theta d\phi \\ &= \sum_{l,m} a_{lm}^* b_{lm} \end{aligned}$$

Calculating the integral with the expansion and compare it with the sinc function we get an error of 10^{-15} .

These tests show that the routines that calculate the expansion work properly. Now that we are confident that the expansions are executed correctly we can use it for some observations. We are interested in equation (3.30) which could be rewritten as

$$t^{exp}(\xi, \zeta) = \sum_{l=0}^{\infty} (\lambda_l - l) \sum_{m=-l}^{m=l} a_{lm}^*(\xi, \zeta) b_{lm}(\zeta) \quad (3.34)$$

and in particular when $\xi = 0$. It can be shown that $b_{lm} = (-1)^l b_{lm}^-$. Moreover, $b_{lm} = (-1)^m b_{l(-m)}^*$ and if $\xi = 0$ then $a_{lm} = b_{lm}^-$. All together, if $\xi = 0$ we have

$$\begin{aligned} a_{lm}^* &= (-1)^m a_{l(-m)} = (-1)^m b_{l(-m)}^- \\ &= (-1)^m (-1)^l b_{l(-m)} = (-1)^{l+m} b_{l(-m)} \end{aligned}$$

which leads to

$$\begin{aligned} \sum_{m=-l}^l a_{lm}^* b_{lm} &= \sum_{m=-l}^l (-1)^{l+m} b_{l(-m)} b_{lm} \\ &= (-1)^l b_{l0}^2 + 2 \sum_{m=1}^l (-1)^{l+m} b_{l(-m)} b_{lm} \end{aligned} \quad (3.35)$$

Observations of the data show that if $\zeta^2 = 0$ then the sum in equation (3.35) is zero for $l > 0$. This is not obvious since the values of $b_{l(-m)} b_{lm}$ for different m seem unrelated. Writing out $b_{l(-m)} b_{lm}$ we get

$$\begin{aligned} b_{lm} b_{l(-m)} &= N_l^m \int_0^\pi P_l^m(\cos \theta) \sin \theta \int_0^{2\pi} e^{-im\phi} f_\zeta(\theta, \phi) d\phi d\theta \\ &\quad N_l^{-m} \int_0^\pi P_l^{-m}(\cos \theta') \sin \theta' \int_0^{2\pi} e^{im\phi'} f_\zeta(\theta', \phi') d\phi' d\theta' \\ &= N_l^m \int_0^\pi P_l^m(\cos \theta) \sin \theta \int_0^{2\pi} e^{-im\phi} f_\zeta(\theta, \phi) d\phi d\theta \\ &\quad N_l^m \int_0^\pi (-1)^m P_l^m(\cos \theta') \sin \theta' \int_0^{2\pi} e^{im\phi'} f_\zeta(\theta', \phi') d\phi' d\theta' \end{aligned}$$

where $f_\zeta(\theta, \phi) = e^{i(\zeta_1 r \sin \theta \cos \phi + \zeta_2 r \sin \theta \sin \phi + \zeta_3 r \cos \theta)}$. Using equation (3.35) in (3.34) we are left with $t^{exp}(0) = (\lambda_0 - 0) b_{00}^2$. But we established in Lemma 3.2.4 that $\lambda_0 = 0$ which makes $t^{exp}(0) = 0$.

Theoretical Considerations

The only expression that we have for t^{exp} is a boundary integral that involves the DtN map. Our knowledge of the DtN map is limited to the knowledge of the eigenvalues and eigenfunctions which leads to the spherical harmonic expansions that we can not solve analytically. Therefore we have a look at Nachman's way to express it, see equation (3.9)

$$t^{exp}(\xi, \zeta) = \int_{\partial D} e^{-ix \cdot (\xi + \zeta)} \Lambda_q e^{ix \cdot \zeta} d\sigma(x) + \int_{\partial D} e^{-ix \cdot \xi} i(\xi + \zeta) \cdot \nu d\sigma(x)$$

which has at least one part that does not involve the DtN map. Evaluating that part at $\xi = 0$ gives

$$\begin{aligned} \int_{\partial D} e^{-ix \cdot 0} i(0 + \zeta) \cdot \nu d\sigma(x) &= i \int_{\partial D} \zeta \cdot \nu d\sigma(x) \\ &= i \int_0^\pi \int_0^{2\pi} [\zeta_1 \sin \theta \cos \phi + \zeta_2 \sin \theta \sin \phi + \zeta_3 \cos \theta] \sin \theta d\phi d\theta \\ &= i \int_0^\pi \sin \theta \left(\zeta_3 \cos \theta + \zeta_1 \sin \theta \int_0^{2\pi} \cos \phi d\phi + \zeta_2 \sin \theta \int_0^{2\pi} \sin \phi d\phi \right) d\theta \\ &= i \int_0^\pi \zeta_3 \sin \theta \cos \theta d\theta = 0 \end{aligned}$$

On the other hand, we have that

$$\begin{aligned} \int_{\partial D} e^{-ix \cdot \xi} i(\xi + \zeta) \cdot \nu d\sigma(x) &= \int_{\partial D} e^{-ix \cdot (\xi + \zeta)} \Lambda_0 e^{ix \cdot \zeta} d\sigma(x) \\ &= \sum_{l,m} l a_{lm}^* b_{lm} \end{aligned}$$

Combing the last two equations we get

$$0 = \int_{\partial D} i\zeta \cdot \nu d\sigma(x) = \int_{\partial D} e^{-ix \cdot \zeta} \Lambda_0 e^{ix \cdot \zeta} d\sigma(x) = \sum_{l,m} l b_{lm}^* b_{lm}$$

which is the same as what we observed with our data if $\zeta^2 = 0$. Note that $\int_{\partial D} i(\xi + \zeta) \cdot \nu d\sigma(x) = \int e^{-ix \cdot \zeta} \Lambda_0 e^{ix \cdot \zeta} d\sigma(x)$ only when $(\xi + \zeta)^2 = 0$. Thus if

$\xi = 0$ we need $\zeta^2 = 0$. We also know that $\lambda_l = |l| + \epsilon$ with ϵ exponentially small, see [67]. This implies that

$$t^{exp} = \sum_{l,m} (\lambda_l - l) b_{lm}^{*-} b_{lm} = \sum_{l,m} \epsilon b_{lm}^{*-} b_{lm}$$

but this expression is small if ϵ is small which implies that $t^{exp}(0)$ is nearly zero.

We can conclude that $t^{exp}(\xi) \neq t(\xi, \zeta)$ for $|\xi|$ close to zero. The remaining question is how this difference influences the reconstruction of $q(x)$ and $\gamma(x)$, which can be seen in the next two sections. Independently of how well t^{exp} reconstructs γ it would be interesting to investigate the possibility to evaluate $t(\xi, \zeta)$ without the use of the asymptotic behavior. That is, instead calculate the scattering data $t(\xi, \zeta)$ with $\psi(x, \zeta)$ which can be determined via equation (3.8).

3.5.4 The Schrödinger Potential

Using $t^{exp}(\xi)$, $t^{LS}(\xi, \zeta_F)$ and $\hat{q}(\xi)$ we can reconstruct three different approximations of the Schrödinger potential $q(x)$ which are displayed in figure 3.5. The black line is the Schrödinger potential calculated from $\gamma(x)$ by $q(x) = \Delta\sqrt{\gamma}/\sqrt{\gamma}$.

First we observe that $q(x)$ and $\mathcal{F}^{-1}(\hat{q}(x))$ look identical which just shows that the implemented routines work properly. The Schrödinger potential, $q^{LS}(x)$, calculated from t^{LS} does not differ much from the target either. The most interesting part is $q^{exp}(x)$, the reconstruction from $t^{exp}(\xi)$. For x close to the boundary we get really good agreement with the target $q(x)$ but for x close to zero we see large discrepancies, especially in the magnitude. Looking at the scattering data in figure 3.4, we see two features that are most likely responsible for that difference. The first one is the

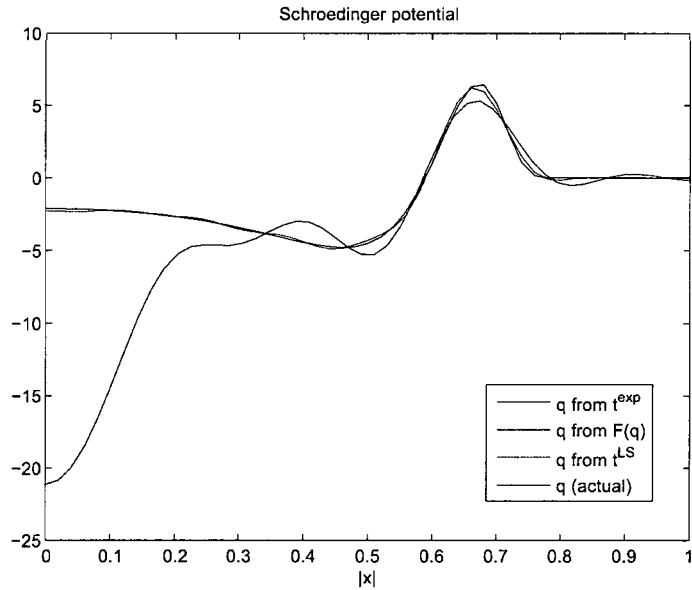


Figure 3.5: Reconstructions of the Schrödinger potential $q(x)$ by taking the inverse Fourier transform of $t^{exp}(\xi)$, $t^{LS}(\xi, \zeta_F)$ and $\hat{q}(\xi)$ and the actual $q(x)$ (black line) for $\alpha = 0.3$ and $d = .9$.

differences in the values of $t^{exp}(\xi)$ for ξ close to zero compared to $\hat{q}(\xi)$. The second is the truncation of $t^{exp}(\xi)$ due to numerical instability for large ξ values. For more details on the influence of the truncation of the scattering data see section 3.5.6.

3.5.5 The Conductivity Distribution

The square root of the reconstructed conductivity distribution $\gamma(x)$ is depicted in figure 3.6. Three of the four displays curves look identical, namely the target and γ calculated from $\mathcal{F}^{-1}(\mathcal{F}(q(x)))$ and γ calculated from $q^{LS}(x)$. The slight difference in the Schrödinger potential $q(x)$ and $q^{LS}(x)$ seems to disappear in the reconstruction of the conductivity. This makes sense considering that the operation is very smoothing. Again, the most

interesting reconstruction is $\gamma^{exp}(x)$. Considering the relatively large difference in magnitude of $q^{exp}(x)$, the reconstructed conductivity distribution is fairly good. A positive aspect is that we get $\gamma \equiv 1$ close to the boundary. Moreover, the overall shape is also fairly well reconstructed. However, the magnitude close to $x = 0$ is off. We still need to keep in mind that γ^{exp} is the only reconstruction that does not use the knowledge of γ explicitly. Implicitly it is in the eigenvalues which serve as our DtN map.

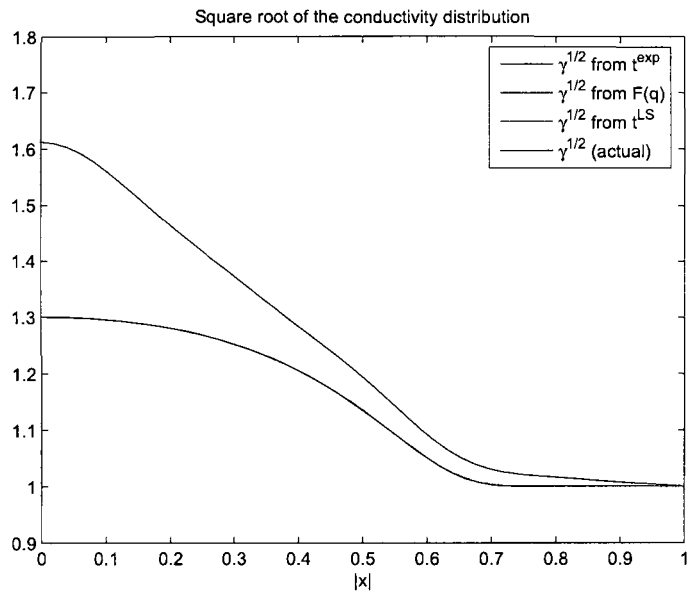


Figure 3.6: The square root of the reconstructed conductivity distribution with parameter $d = 0.9$ and $\alpha = 0.3$. The reconstructions from t^{LS} and \hat{q} are identical with $\sqrt{\gamma(x)}$.

3.5.6 The Influence of Different Parameters

The Influence of the Truncation of the Scattering data

When we reconstructed q^{exp} and γ^{exp} we truncated the scattering data t^{exp} due to numerical instabilities. In this section we investigate the influ-

ence of the truncation of the scattering data using the scattering data t^{LS} calculated by equation (3.4). Figure 3.7 shows $t^{LS}(\xi, \zeta_F)$ and the reconstruc-

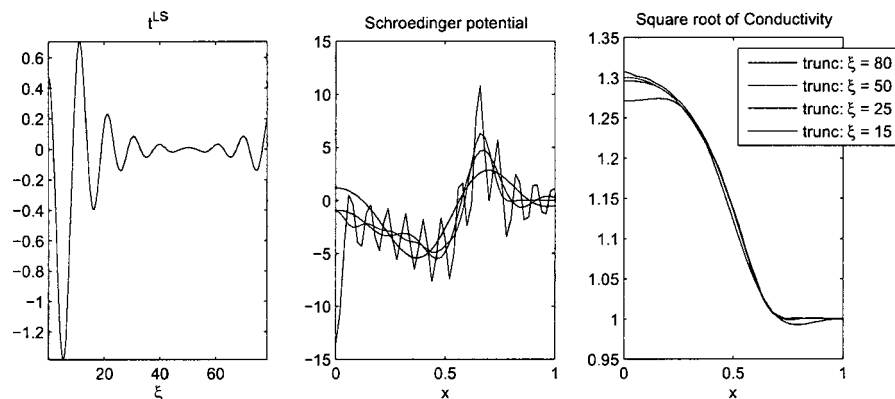


Figure 3.7: The first plot shows the scattering data t^{LS} . From this the Schrödinger potential was determined with different truncation, $\xi = 80$ (black), 50 (green), 25 (red) and 15 (blue), respectively. The reconstructions $q(x)$ are displayed in the second plot. The third plot shows the square root of γ calculated from the different Schrödinger potentials.

tions $q(x)$ and $\sqrt{\gamma(x)}$ for different truncations of t^{LS} . First observe that t^{LS} is not perfectly reconstructed for large ξ 's. This could be changed by setting the calculation of t^{LS} to be more accurate⁷. Different $q(x)$ were computed from $t^{LS}(\xi, \zeta_F)$ by truncating at $\xi = 15$, $\xi = 25$, $\xi = 50$ and $\xi = 80$ (no truncation). The second plot in figure 3.7 displays the results. The most unexpected reconstruction is that of $q(x)$ from t^{LS} with no truncation. It oscillates but the general shape is still recognizable. The oscillation comes from the inaccurate $t^{LS}(\xi, \zeta_F)$ values for large ξ . The computed conductivity is shown in the third plot of figure 3.7. All reconstructions are very good.

⁷Since this calculation is not part of this thesis and was realized by Kim Knudsen we do not go into more details.

The reconstruction of γ from t^{LS} with no truncation shows nearly no difference from the actual value of γ even though the corresponding Schrödinger potentials differ. The only reconstruction showing a noticeable difference is the one for which we truncate t^{LS} most. Despite the large truncation the reconstruction of γ is very good, implying that for the reconstruction of γ the values of the scattering data for small ξ are very important.

The Influence of the Support of γ

So far we considered reconstructions with fixed values for d and α , which determine the support and the magnitude of $\gamma(x)$. Figure 3.8 displays reconstructions with different support of γ , that is different d -values in each row. The first column shows $t^{exp}(\xi)$ in red and $\hat{q}(\xi)$ in blue as a reference. The Schrödinger potential is presented in the second column and the square root of the reconstructed conductivity can be observed in column three. The red lines are the reconstructions and the blue ones are the target values. From the last column we can conclude that we get more accurate reconstructions with conductivities that have small support. With $d = .3$ we get very good reconstruction from the approximation of the scattering data $t^{exp}(\xi)$.

The Influence of the Magnitude of γ

It still remains to investigate the influence of the parameter α , which determines the magnitude of the conductivity distribution. Figure 3.9 displays reconstructions of the square root of $\gamma(x)$ from $t^{exp}(\xi)$ for different support and magnitude of γ . Each row correspond to a certain d -value and each column to a specific α -value. The red curves show the reconstructions whereas the blue curves are the actual values, $\sqrt{\gamma}$. As in figure 3.8 we see

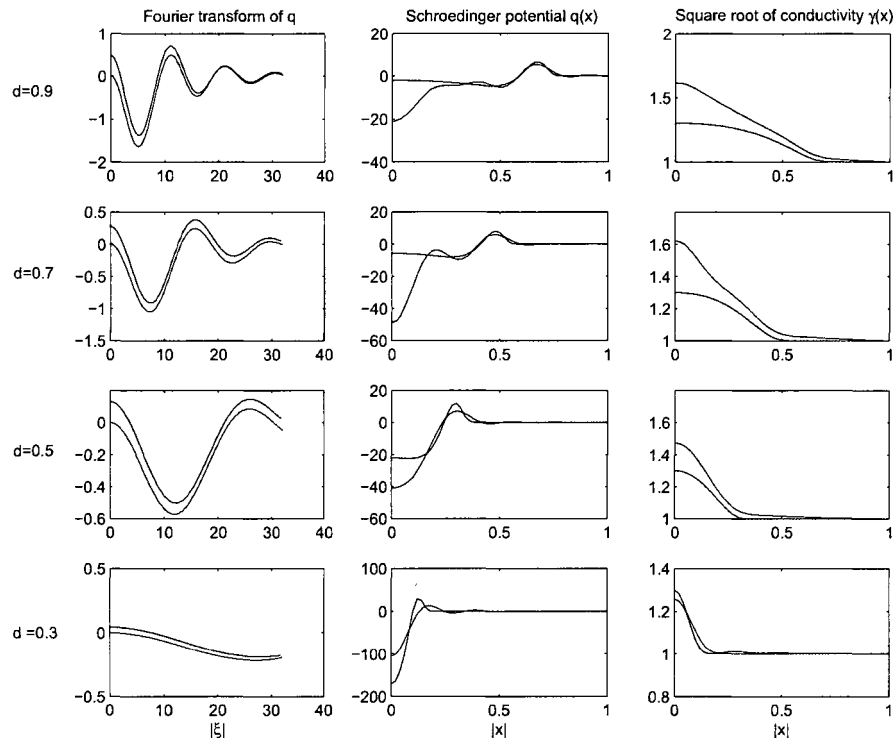


Figure 3.8: Each row represents a different support of γ , namely .9, .7, .5, .3. The red curve in the first column is $t^{exp}(\xi)$ and the blue one is the Fourier transform of $q(x)$. The second column is the Schrödinger potential, $q(x)$ and the third column displays the square root of the conductivity $\gamma(x)$. The red curves displays the reconstructions from t^{exp} and the blue curves the actual values γ .

again that the reconstructions are better if γ has a small support. Moreover, we observe that smaller magnitudes can be reconstructed much better than larger ones. Even though conductivities with small support and small magnitude are reconstructed extremely well, the reconstructions get worse very quickly.

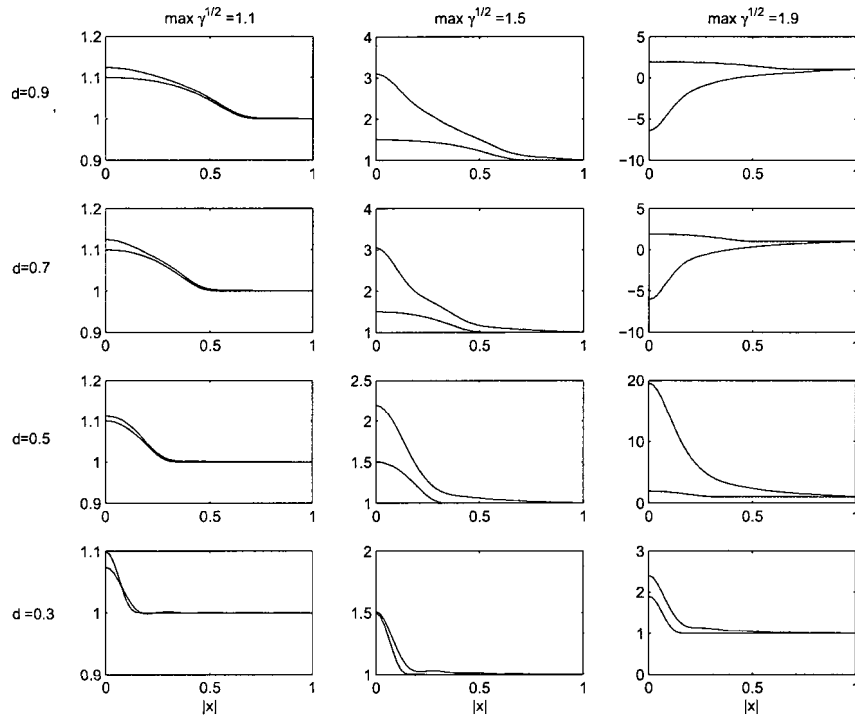


Figure 3.9: Reconstructions from t^{exp} for different support and magnitude of γ . Each row corresponds to a specific d , namely .9, .7, .5, .3 and each column correspond to a specific magnitude of γ . The blue curves are the actual values and the red ones are the reconstructed.

3.6 Conclusion

We implemented a first version of a direct EIT reconstruction algorithm on a spherical domain and considered spherically symmetric conductivity distributions. An approximation of the eigenvalues of the DtN map in connection with the eigenfunctions served as the DtN map and the asymptotic behavior of the exponentially growing solutions was used to calculate an approximation of the scattering data, t^{exp} . The second part of the algorithm computes the Schrödinger potential $q(x)$ by taking the inverse Fourier

transform of the large $|\zeta|$ limit of the scattering data. The last step solves equation (3.12) to determine the conductivity distribution $\gamma(x)$ from $q(x)$.

Given a good approximation of the scattering data such as the scattering transform $t^{LS}(\xi, \zeta)$ computed from the forward problem or the Fourier transform of $q(x) = \Delta\sqrt{\gamma}/\sqrt{\gamma}$ we can reconstruct the Schrödinger potential $q(x)$ and conductivity distribution $\gamma(x)$ with good accuracy.

The approximation of the scattering data $t^{exp}(\xi, \zeta)$ calculated from the DtN map differs from the actual scattering data, $t(\xi, \zeta)$ close to $\xi = 0$. At exactly $\xi = 0$ we have $t(0, \zeta) = \hat{q}(0)$ which is in general not equal to zero as $t^{exp}(0)$ is. Consequently the reconstructions of the Schrödinger potential and the conductivity distribution are poor. Encouraging are the good values of $t^{exp}(\xi, \zeta)$ for $|\zeta|$ large but small enough to avoid instabilities and the relative good spatial resolution of $\gamma(x)$. Furthermore, the values of $q(x)$ and $\gamma(x)$ reconstructed from t^{exp} are excellent near the boundary.

3.7 Directions for Future Research

This work is a starting point in the implementation of a direct reconstruction method in three dimensions, which means that there are many open questions and directions of research.

I think the next step should be the determination of the scattering data from boundary measurements using the exponentially growing solutions which can be calculated via equation (3.8). I would like to see how the use of the exponential growing solutions in the calculation of the scattering data influences the results.

Once we have the scattering data, further ideas can be explored. The following includes some ideas how to advance the 3D direct method so that hopefully one day it can be used in clinical settings.

- **The $\bar{\partial}$ -Equation** If the scattering data is given we can reconstruct the conductivity distribution using the ‘large’ ζ limit. The problem is that we have $\psi(x, \zeta) \approx e^{ix\zeta}$ and if $|\zeta|$ is large, this function is highly oscillatory. We can expect that this might cause problems in the calculation of the scattering data. To avoid oscillations in $\psi(x, \zeta)$, we would like to implement the $\bar{\partial}$ -method suggested in [24] because this algorithm requires $|\zeta|$ small.
- **Including Electrodes** In this work we assumed the boundary data to be continuous. This is not a realistic assumption since in practice, electrodes are used, which makes the boundary data discrete. With the inclusion of electrodes we introduce several new questions, including that of electrode placement, choosing an electrode model, the choice of current patterns, as well as the adjustment of the calculation of the DtN map to accommodate these changes. One idea is, for example, the application of the eigenfunctions of the DtN map as current patterns. That would allow us to use most of the derivation in this work.
- **Different Domains** We considered in this work spherical domains, keeping in mind application such as breast cancer detection and imaging conductivity changes in the brain. Conceivably, there are other scenarios. We could consider a cube which lies beneath a planar electrode array or between two parallel planar electrode arrays. see for example [15]. Moreover, independent of the basic shape of the domain we need take into account that these shapes vary from person to person somewhat in size and shape. Ideas could be drawn from the work in two dimensions, see, for example [61].

- **Partial Data** Another problem in applications is that we have only partial boundary measurements. For example, the head is not accessible from all sides. This raises first the question of whether it is possible to reconstruct the conductivity distribution from partial knowledge of the DtN map, and second how can this be done. The first question is answered for example in [45] for 2D. See also references therein.

Chapter 4

SUMMARY

In this thesis we investigated two different reconstructions algorithms that take voltage and current density measurements from the boundary and determine the electrical conductivity distribution within the object. The conductivity is then displayed as an image. With such techniques it is possible to ‘look inside’ an unknown object such as a human body or below the surface of the earth. The long term goal is to develop fast, robust and reliable algorithms that can be used in commercial and/or clinical settings and might help, for example, to diagnose diseases.

The contribution of this thesis towards 2D reconstructions is the investigation of a 2D linearization method that is fast and gives very good results. The work is published in [11] and is described in chapter 2.

The contribution of this thesis towards 3D reconstruction is the study of a 3D direct reconstruction method and its implementation. Since the algorithm outlined in [62] solves the full nonlinear problem without iterations, it has the potential for very accurate reconstructions. As a result of this study we conclude that the approximations to the scattering transform that were successfully used in 2D show limited success in the three dimensional setting. In addition, this work provides a framework for the algorithm which

could be utilized for further improvements and serve as a basemark for assessing whether the alterations are actual improvements or not. Another result of this study is the successful reconstruction of Schrödinger potentials and conductivity distributions from accurate scattering data. Overall we are optimistic that with some improvements this algorithm will provide good reconstruction for three dimensional objects.

Appendix A

CALCULATION OF THE ERROR BOUND IN CALDERÓN'S METHOD

We will use the usual notation for the Hilbert-Sobolev spaces, also called H -spaces. Recall that the norm of a function $f(x)$ in $H^1(D)$ is

$$\|f(x)\|_{H^1} = (\|f(x)\|_{L^2}^2 + \|\nabla f(x)\|_{L^2}^2)^{1/2}.$$

The space $H_0^1(D)$ of functions in H^1 whose trace is zero on the boundary ∂D almost everywhere will be endowed with the norm

$$\|f(x)\|_{H_0^1} = \left(\int_D |\nabla f(x)|^2 dx \right)^{1/2} = \|\nabla f(x)\|_{L^2} \quad (\text{A.1})$$

which is equivalent to $\|f(x)\|_{H^1}$.¹ Members u^* of the dual space of H_0^1 , denoted H^{-1} , act on functions in H_0^1 and have norm

$$\|u^*\|_{H^{-1}} = \sup_{\|u\| \leq 1} |u^*(u)|.$$

For the trace of a solution u to the conductivity equation, Calderón uses the norm

$$\|\Phi\|^2 = \int_D |\nabla u|^2 dx, \quad u|_{\partial D} = \Phi, \quad \Delta u = 0 \quad \text{in } D \quad (\text{A.2})$$

¹This can be shown with the Poincaré Inequality. See for example [57]

Calderón proved that the linearization of Q is injective, and therefore (A.2) does define a norm on $\Phi \in H^{\frac{1}{2}}$.

Consider $v \in H_0^1(D)$ defined as in section 2.1.1 and L_1v as an operator from $H_0^1(D)$ into $H^{-1}(D)$. Such an operator is an isomorphism if the domain D is bounded (see for example [57].) Let G denote the inverse of the operator L_1v and

$$A = \|G\|_{H^{-1} \rightarrow H^1} < \infty. \quad (\text{A.3})$$

Let $w \in H^1$ and consider the operator $L_\delta w : H_0^1 \rightarrow \mathbb{R}$ given by $L_\delta w(v) = \int_D v \nabla \cdot \delta \nabla w \, dx$. This is a linear functional, and we can use the operator norm of linear operators to show that it is bounded. Integration by parts and Hölder's inequality give

$$\begin{aligned} \left| \int_D (\nabla \cdot \delta \nabla w) v \, dx \right| &\leq \|\delta \nabla w\|_{L^2}^2 \|\nabla v\|_{L^2}^2 \\ &\leq \|\delta\|_\infty \|\nabla w\|_{L^2} \|\nabla v\|_{L^2} \\ &= \|\delta\|_\infty \|\nabla w\|_{L^2} \|v\|_{H_0^1}. \end{aligned}$$

This implies that $L_\delta w \in H^{-1}(D)$ since it is a linear bounded functional on H_0^1 . Thus

$$\begin{aligned} \|L_\delta w\|_{H_0^1 \rightarrow \mathbb{R}} &\equiv \sup_{v \in H_0^1} \frac{|\int_D (\nabla \cdot \delta \nabla w) v \, dx|}{\|v\|_{H_0^1}} \\ &\leq \frac{\|\delta\|_\infty \|\nabla w\|_{L^2} \|v\|_{H_0^1}}{\|v\|_{H_0^1}} = \|\delta\|_\infty \|\nabla w\|_{L^2}. \end{aligned}$$

To find a bound on v , note that by the reverse triangle inequality

$$\|v + GL_\delta v\|_{H^1} = \|v - (-GL_\delta v)\|_{H^1} \geq \|v\|_{H^1} - \|-GL_\delta v\|_{H^1}$$

and

$$\begin{aligned} \|-GL_\delta v\|_{H^1} &\leq \|-G\|_{H^{-1} \rightarrow H^1} \|L_\delta v\|_{H_0^1 \rightarrow \mathbb{R}} \\ &= A \|\delta\|_\infty \|\nabla v\|_{L^2} = A \|\delta\|_\infty \|v\|_{H_0^1}. \end{aligned}$$

Hence

$$\begin{aligned}
\|v + GL_\delta v\|_{H^1} &\geq \|v\|_{H^1} - \| -G\|_{H^{-1} \rightarrow H^1} \|L_\delta v\|_{H_0^1 \rightarrow \mathbb{R}} \\
&\geq \|v\|_{H^1} - A \|\delta\|_\infty \|v\|_{H^1} \\
&= (1 - A \|\delta\|_\infty) \|v\|_{H^1}.
\end{aligned}$$

Now applying (2.3), $L_\delta v = -L_\delta u - L_1 v$,

$$\begin{aligned}
(1 - A \|\delta\|_\infty) \|v\|_{H^1} &\leq \|v + GL_\delta v\|_{H^1} = \|GL_\delta u\|_{H^1} \\
&\leq A \|L_\delta u\|_{H_0^1 \rightarrow \mathbb{R}} \\
&\leq A \|\delta\|_\infty \|\nabla u\|_{L^2} \\
&= A \|\delta\|_\infty \left(\int_D |\nabla u|^2 dx \right)^{\frac{1}{2}} \\
&= A \|\delta\|_\infty \|\Phi\|
\end{aligned}$$

Thus

$$(1 - A \|\delta\|_\infty) \|v\|_{H^1} \leq \|v + GL_\delta v\|_{H^1} \leq A \|\delta\|_\infty \|\Phi\|$$

leads to

$$\|v\|_{H^1} \leq \frac{A \|\delta\|_\infty \|\Phi\|}{1 - A \|\delta\|_\infty}. \quad (\text{A.4})$$

Now we can go on and derive a bound for the remainder $R(z) = \frac{1}{2\pi^2|z|^2} \int_D \delta \nabla u_2 \cdot \nabla v_1 dx$. By the Cauchy-Schwartz inequality

$$\begin{aligned}
|R(z)| &\leq \frac{\|\delta\|_\infty}{2\pi^2|z|^2} \|\nabla u_2\|_{L^2} \|\nabla v_1\|_{L^2} \\
&\leq \frac{\|\delta\|_\infty}{2\pi^2|z|^2} \|\Phi_2\| \|v_2\|_{H^1} \\
&\leq \frac{1}{2\pi^2|z|^2} \frac{A \|\delta\|_\infty^2 \|\Phi_1\| \|\Phi_2\|}{1 - A \|\delta\|_\infty} \\
&\leq \frac{1}{2\pi^2|z|^2} \frac{A \|\delta\|_\infty^2 \|\Phi_1\| \|\Phi_2\|}{\epsilon} \quad (\text{A.5})
\end{aligned}$$

if $A\|\delta\|_\infty < 1 - \epsilon$. Using the definition of the norm of Φ (A.2) and the functions introduced in equation (2.4) with $(a \cdot z) = 0$ and $|z| = |a|$ we get

$$\begin{aligned}
& \|\Phi_1\| \|\Phi_2\| & (A.6) \\
& \leq \|(i\pi z + \pi a)e^{i\pi(z \cdot x) + \pi(a \cdot x)}\| \|(i\pi z - \pi a)e^{i\pi(z \cdot x) - \pi(a \cdot x)}\| \\
& = |i\pi z + \pi a| |i\pi z - \pi a| \|e^{i\pi(z \cdot x)} e^{\pi(a \cdot x)}\| \|e^{i\pi(z \cdot x)} e^{-2\pi(a \cdot x)}\| \\
& \quad \text{using } |e^{ik}| \leq 1 \quad \text{and } e^{(a \cdot x)} \leq e^{|a \cdot x|} \leq e^{|a||x|} \\
& \leq (\pi|z| + \pi|a|)(\pi|z| + \pi|a|) \left(\int_D e^{2\pi|a|r} dx \right)^{\frac{1}{2}} \left(\int_D e^{2\pi|a|r} dx \right)^{\frac{1}{2}} \\
& \leq 2\pi^2|z|^2 e^{2\pi|a|r} * (\text{area of } D) & (A.7)
\end{aligned}$$

where r is the radius of the smallest sphere containing D . Let $C = \frac{1}{\epsilon} A * (\text{area of } D)$. Then equation (A.5) together with (A.7) gives

$$|R(z)| \leq C \|\delta\|_\infty^2 e^{2\pi|z|r}$$

which is the given error bound.

Bibliography

- [1] A. Adler, R. Amyot, R. Guardo, J. H. Bates, and Y. Berthiaume. Monitoring changes in lung air and liquid volumes with electrical impedance tomography. *J. Appl. Physiol.*, 83(5):1762–1767, 1997.
- [2] A. Allersi and F. Santosa. Stability and resolution analysis of a linearized problem in electrical impedance tomography. *Inverse Problems*, 7(4):515–533, 1991.
- [3] G. B. Arfken and H. J. Weber. *Mathematical Methods for Physicists*. Academic Press, 2001.
- [4] M. Assenheimer, O. Laver-Moskovitz, D. Malonek, D. Manor, U. Nahaliel, R. Nitzan, and A. Saad. The t-scan technology: electrical impedance as a diagnostic tool for breast cancer detection. *Physiol. Meas.*, 22(1):1–8, 2001.
- [5] K. Astala and L. Päivärinta. Calderón’s inverse conductivity problem in the plane. *Ann. of Math. (2)*, 163(1):265–299, 2006.
- [6] A. P. Bagshaw, A. D. Liston, R. H. Bayford, A. Tizzard, A. P. Gibson, A. T. Tidswell, M. K. Sparkes, H. Dehghani, C. D. Binnie, and D. S. Holder. Electrical impedance tomography of human brain function using reconstruction algorithms based on the finite element method. *NeuroImage*, 20(2):752–764, 2003.
- [7] D. C. Barber and B. H. Brown. Applied potential tomography. *Journal of Physics E: Scientific Instruments*, 17(9):723–733, 1984.
- [8] D. C. Barber and B. H. Brown. Progress in electrical impedance tomography. In *Inverse Problems in Partial Differential Equations*, Philadelphia. SIAM, 1990.
- [9] C. Berenstein and E. C. Tarabusi. Inversion formulas for the k -dimensional radon transform in real hyperbolic spaces. *Duke Math. J.*, 62:1–19, 1991.

- [10] J. Bikowski and J. L. Mueller. Electrical impedance tomography and fast multipole method. In *Proceedings of SPIE 49th Annual Meeting, Denver, 2004*.
- [11] J. Bikowski and J. L. Mueller. 2D EIT reconstructions using Calderón's method. *Inverse Probl. Imaging*, 2(1):43–61, 2008.
- [12] R. Blue. *Real-time three-dimensional electrical impedance tomography*. PhD thesis, R.P.I., Troy, NY, 1997.
- [13] L. Borcea. Nonlinear multigrid for imaging electrical conductivity and permittivity at low frequency. *Inverse Problems*, 17:329–359, 2001.
- [14] L. Borcea, J. G. Berryman, and G. Papanicolaou. High contrast impedance tomography. *Inverse Problems*, 12:835–858, 1996.
- [15] G. Boverman, T. Kao, D. Isaacson, and G. J. Saulnier. An implementation of calderón's method for 3-d limited-view eit. *IEEE Transactions on Medical Imaging*, 2009.
- [16] E. O. Brigham. *The Fast Fourier Transform*. Prentice Hall, Inc, 1974.
- [17] R. M. Brown and R. H. Torres. Uniqueness in the inverse conductivity problem for conductivities with $3/2$ derivatives in L^p , $p > 2n$. *J. Fourier Anal. Appl.*, 9(6):563–574, 2003.
- [18] A. P. Calderón. On an inverse boundary value problem. In *Seminar on Numerical Analysis and its Applications to Continuum Physics*, pages 65–73. Soc. Brasileira de Matemática, 1980.
- [19] M. Cheney, D. Isaacson, and E. L. Isaacson. Exact solutions to a linearized inverse boundary value problem. *Inverse Problems*, 6:923–934, 1990.
- [20] M. Cheney, D. Isaacson, and J. C. Newell. Electrical impedance tomography. *SIAM Review*, 41(1):85–101, 1999.
- [21] M. Cheney, D. Isaacson, J. C. Newell, J. Goble, and S. Simske. Noser: and algorithm for solving the inverse conductivity problem. *Internat. J. Imaging Systems and Technology*, 2:66–75, 1990.
- [22] V. A. Cherepenin, A. Y. Karpov, A. V. Korjnevsky, V. N. Kornienko, Y. S. Kultiasov, M. B. Ochapkin, O. V. Trochanova, and J. D. Meister. Three-dimensional eit imaging of breast tissues: system design and clinical testing. *IEEE Trans Med Imaging*, 21(6):662–667, 2002.

- [23] M. H. Choi, T. Kao, D. Isaacson, G. J. Saulnier, and J. C. Newell. A reconstruction algorithm for breast cancer imaging with electrical impedance tomography in mammography geometry. *IEEE Transactions on Biomedical Engineering*, 54(4):700–710, 2007.
- [24] H. Cornean, K. Knudsen, and S. Siltanen. Towards a d -bar reconstruction method for three-dimensional EIT. *J. Inverse Ill-Posed Probl.*, 14(2):111–134, 2006.
- [25] Jr. D. N. Healy, D. N. Rockmore, P. J. Kostelec, and S. Moore. FFTs for the 2-sphere-improvements and variations. *J. Fourier Anal. Appl.*, 9(4):341–385, 2003.
- [26] D. C. Dobson. Convergence of a reconstruction method for the inverse conductivity problem. *SIAM J. Appl. Math.*, 52(2):442–458, 1992.
- [27] D. C. Dobson and F. Santosa. An image-enhancement technique for electrical impedance tomography. *Inverse Problems*, 10:317–334, 1994.
- [28] O. Dorn, H. Berteta-Aguirre, J. G. Berryman, and G. Papanicolaou. A nonlinear inversion method for 3d-electromagnetic imaging using adjoint fields. *Inverse Problems*, 15:1523–1558, 1999.
- [29] P. Edic, G. J. Saulnier, J. C. Newell, and D. Isaacson. A real-time electrical impedance tomograph. *IEEE Trans. Biomed. Engr.*, 42:849–859, 1995.
- [30] L. C. Evans. *Partial Differential Equations*. American Mathematical Society, 1998.
- [31] L. D. Faddeev. Increasing solutions of the schrödinger equation. *Sov. Phys. Dokl*, 10:1033–1035, 1966.
- [32] I. Frerichs, G. Schmitz, S. Pulletz, D. Schädler, G. Zick, J. Scholz, and N. Weiler. Reproducibility of regional lung ventilation distribution determined by electrical impedance tomography during mechanical ventilation. *Physiol. Meas.*, 28:261–267, 2007.
- [33] H. Fricke and S. Morse. The electric capacity of tumors of the breast. *J. Cancer Res.*, 10:340–376, 1926.
- [34] L. A. Geddes and L. E. Baker. The specific resistance of biological material - a compendium of data for the biomedical engineer and physiologist. *Medical and Biological Engineering and Computing*, 5(3):271–293, 1967.

- [35] D. G. Gisser, D. Isaacson, and J. C. Newell. Electric current tomography and eigenvalues. *SIAM J. Appl. Math.*, 50:1623–1634, 1990.
- [36] B. M. Graham. *Enhancements in Electrical Impedance Tomography (EIT) Image Reconstruction for 3D Lung Imaging*. PhD thesis, School of Information Technology, University of Ottawa, Canada, 2007.
- [37] A. Greenleaf, M. Lassas, and G. Uhlmann. Anisotropic conductivities that cannot be detected in eit. *Physiol. Meas.*, 24:413–420, 2003.
- [38] A. Greenleaf, M. Lassas, and G. Uhlmann. On nonuniqueness for Calderón’s inverse problem. *Math. Res. Lett.*, 10(5-6):685–693, 2003.
- [39] A. Greenleaf, M. Lassas, and G. Uhlmann. Invisibility and inverse problems. *Bull. Amer. Math. Soc.*, 46:55–97, 2009.
- [40] J. Hadamard. Sur les problèmes aux limites partielles et leur signification physique. *Princeton University Bulletin*, pages 49–52, 1902.
- [41] R. J. Halter, A. Hartov, and K. D. Paulsen. Experimental justification for using 3d conductivity reconstructions in electrical impedance tomography. *Physiol. Meas.*, 28:S115–S127, 2007.
- [42] T. E. Hatziafratis. An explicit koppelman type integral formula on analytic varieties. *Michigan Math. J.*, 33:335–341, 1986.
- [43] T. A. Hope and S. E. Iles. Technology review: The use of electrical impedance scanning in the detection of breast cancer. *Breast Cancer Research*, 6(2):69–74, 2004.
- [44] K. B. Howell. *Principles of Fourier analysis*. Studies in Advanced Mathematics. Chapman & Hall/CRC, Boca Raton, FL, 2001.
- [45] O. Imanuvilov, G. Uhlmann, and M. Yamamoto. Global uniqueness from partial cauchy data in two dimensions. preprint.
- [46] D. Isaacson and M. Cheney. Effects of measurement precision and finite numbers of electrodes on linear impedance imaging algorithms. *SIAM J. Appl. Math.*, 15:1705–1731, 1991.
- [47] D. Isaacson, J. L. Mueller, J. C. Newell, and S. Siltanen. Reconstructions of chest phantoms by the d-bar method for electrical impedance tomography. *IEEE Transactions on Medical Imaging*, 23:821– 828, 2004.

- [48] D. Isaacson, J. L. Mueller, and J. C. Newell S. Siltanen. Imaging cardiac activity by the d-bar method for electrical impedance tomography. *Physiol. Meas.*, 27:S43–S50, 2006.
- [49] J. P. Kaipio, V. Kolehmainen, E. Somersalo, and M. Vauhkonen. Statistical inversion and Monte Carlo sampling methods in electrical impedance tomography. *Inverse Problems*, 16(5):1487–1522, 2000.
- [50] J. S. Kallman and J. G. Berryman. Weighted least-squares methods for electrical impedance tomography. *IEEE Trans. Med. Imaging*, 11:284–292, 1992.
- [51] T. E. Kerner, K. D. Paulsen, A. Hartov, S. K. Soho, and S. P. Poplack. Electrical impedance spectroscopy of the breast: clinical imaging results in 26 subjects. *IEEE Trans. Med. Imaging*, 21(6):638–645, 2002.
- [52] K. Knudsen, M. Lassas, J. L. Mueller, and S. Siltanen. D-bar method for electrical impedance tomography with discontinuous conductivities. *SIAM J. Appl. Math.*, 67(3):893–913 (electronic), 2007.
- [53] R. V. Kohn and M. Vogelius. Determining conductivity by boundary measurements ii. interior results. *Communications on Pure and Applied Mathematics*, 38:643–667, 1985.
- [54] P. W. Kunst, A. Vonk Noordegraaf, O. S. Hoekstra, P. E. Postmus, and P. M. de Vries. Ventilation and perfusion imaging by electrical impedance tomography: a comparison with radionuclide scanning. *Physiol. Meas.*, 19(4):481–490, 1998.
- [55] W. Magnus, F. Oberhettinger, and R. P. Soni. *Formulas and Theorems for the Special Functions of Mathematical Physics*. Springer, 1966.
- [56] T. Martin and J. Idier. Estimating a conductivity distribution via a fem-based nonlinear bayesian method. *The European Physical Journal Applied Physics*, 1(1):87–91, 1998.
- [57] R. C. McOwen. *Partial Differential Equations: Methods and Applications*. Prentice Hall, 1996.
- [58] P. Metherall, D. C. Barber, R. H. Smallwood, and B. H. Brown. Three-dimensional electrical impedance tomography. *Nature*, 380:509–512, 1996.
- [59] J. L. Mueller, D. Isaacson, and J. C. Newell. A reconstruction algorithm for electrical impedance tomography data collected on rectangular electrode arrays. *IEEE Trans. Biomed. Engr.*, 49:1379–1386, 1999.

- [60] J. L. Mueller and S. Siltanen. Direct reconstructions of conductivities from boundary measurements. *SIAM J. Sci. Comput.*, 24(4):1232–1266 (electronic), 2003.
- [61] E. Murphy. *I don't know the title*. PhD thesis, Colorado State University, Fort Collins, CO, 2007.
- [62] A. I. Nachman. Reconstructions from boundary measurements. *Annals of Mathematics*, 128:531–576, 1988.
- [63] A. I. Nachman. Global uniqueness for a two-dimensional inverse boundary value problem. *Annals of Mathematics*, 143:71–96, 1996.
- [64] S. Porsiainen. Two-stage reconstruction of a circular anomaly in electrical impedance tomography. *Inverse Problems*, 22(5):1689–1703, 2006.
- [65] F. Santosa and M. Vogelius. A backprojection algorithm for electrical impedance imaging. *SIAM J. Appl. Math.*, 50:216–243, 1990.
- [66] W. Shuai, F. Fu, F. You, X. Shi, R. Liu, and X. Dong. Imaging techniques of electrical impedance tomography for real-time medical monitoring. *Journal of US-China Medical Science*, 4(7):20–23, 2007.
- [67] S. Siltanen, J. L. Mueller, and D. Isaacson. An implementation of the reconstruction algorithm of a. nachman for the 2-d inverse conductivity problem. *Inverse Problems*, 16:681–699, 2000.
- [68] E. Somersalo, M. Cheney, and D. Isaacson. Existence and uniqueness for electrode models for electric current computed tomography. *SIAM J. Appl. Math.*, 52(4):1023–1040, 1992.
- [69] E. Somersalo, M. Cheney, D. Isaacson, and E. Isaacson. Layer stripping: a direct numerical method for impedance imaging. *Inverse Problems*, 7:899–926, 1991.
- [70] S. Stefanescu, C. Schlumberger, and M. Schlumberger. Sur la distribution électrique autour d'une prise de terre ponctuelle dans un terrain a couchés horizontales, homogenes et isotropes. *J. Physics and Radium Ser.*, 7:132–140, 1930.
- [71] J. Sylvester. A convergent layer stripping algorithm for the radially symmetric impedance tomography problem. *Communications in partial differential equations*, 17:1955–1994, 1992.

- [72] J. Sylvester and G. Uhlmann. A global uniqueness theorem for an inverse boundary value problem. *Annals of Mathematics*, 125:153–169, 1987.
- [73] T. Tidswell, A. Gibson, R. H. Bayford, and D. S. Holder. Three-dimensional electrical impedance tomography of human brain activity. *NeuroImage*, 13:283–294, 2001.
- [74] G. Uhlmann. Developments in inverse problems since Calderón’s foundational paper. In *Harmonic analysis and partial differential equations (Chicago, IL, 1996)*, Chicago Lectures in Math., pages 295–345. Univ. Chicago Press, Chicago, IL, 1999.
- [75] P. J. Vauhkonen, M. Vauhkonen, T. Savolainen, and J. P. Kaipio. Static three-dimensional electrical impedance tomography. *Ann New York Acad Sci*, 873:472–481, 1999.
- [76] J. A. Victorino, J. B. Borges, V. N. Okamoto, G. F. J. Matos, M. R. Tucci, M. P. R. Carames, H. Tanaka, F. S. Sipmann, D. C. B. Santos, C. S. V. Barbas, C. R. R. Carvalho, and M. B. P. Amato. Imbalances in regional lung ventilation: a validation study on electrical impedance tomography. *American Journal of Respiratory and Critical Care Medicine*, 169:791–800, 2004.
- [77] R. M. West, R. G. Aykroyd, S. Meng, and R. A. Williams. Markov chain monte carlo techniques and spatial-temporal modelling for medical eit. *Physiol. Meas.*, 25(1):181–194, 2004.
- [78] A. E. Yagle. A layer stripping fast algorithm for the two-dimensional direct current inverse resistivity problem. *IEEE Trans. Geosci. Remote Sensing*, 25:558–563, 1987.